doi:10.26443/seismica.v2i4.1163

Evidence for an active transtensional Beaufort Range fault in the northern Cascadia forearc

Emerson M. Lynch * [1], **Christine Regalla** [1], **Kristin Morell** [2], **Nicolas Harrichhausen** [3], **Lucinda J. Leonard** [4]

[1]School of Earth and Sustainability, Northern Arizona University, Flagstaff, AZ, USA, [2]Department of Earth Science, University of California, Santa Barbara, CA, USA, [3]Department of Geological Sciences, University of Alaska, Anchorage, AK, USA, [4]School of Earth and Ocean Sciences, University of Victoria, Victoria, BC, Canada

Author contributions: *Methodology*: Emerson Lynch, Christine Regalla. *Software*: Emerson Lynch. *Validation*: Christine Regalla. *Formal Analysis*: Emerson Lynch, Christine Regalla, Kristin Morell. *Investigation*: Emerson Lynch, Christine Regalla, Kristin Morell, Nicolas Harrichhausen, Lucinda Leonard. *Writing - Original draft*: Emerson Lynch, Christine Regalla. *Writing - Review & Editing*: Emerson Lynch, Christine Regalla, Kristin Morell, Nicolas Harrichhausen, Lucinda Leonard. *Visualization*: Emerson Lynch, Christine Regalla. *Funding acquisition*: Christine Regalla, Kristin Morell.

Abstract Geologic records of fault slip in subduction forearcs provide critical data on stress and strain in the upper plate and the seismogenic potential of hazardous faults. However, few active upper-plate faults have been identified in the northern Cascadia forearc. Here we investigate the slip history of the Beaufort Range fault (BRF) on Vancouver Island, BC, Canada, a proposed source of the 1946 M 7.3 Vancouver Island earthquake, the largest recorded in Cascadia. We use recently-collected lidar data, field mapping, and surveying of offset landforms to map the extent of previously unidentified post-glacial (<14 ka) tectonic scarps and reconstruct 3D fault slip vectors. Post-glacial landforms show increasing displacement with age, suggesting at least three M_W ~6.5–7.5 earthquakes since ~14 ka, the most recent <4 ka. These displacements suggest the BRF is one of the fastest-slipping faults in the northern Cascadia forearc (0.5–2 mm/yr). Kinematic slip inversions of offset geomorphic piercing lines are consistent with right-lateral transtension along a steeply NE-dipping fault. Because BRF fault geometry and kinematics are similar to the 1946 earthquake, it is a plausible source. The kinematic similarity of millennial and decadal slip data suggests the BRF has accommodated transtension over multiple earthquake cycles.

Non-technical summary Subduction zones, like Cascadia, contain onshore fault networks that can host earthquakes that are dangerous to communities. However in many locations, like Vancouver Island, Canada, we know little about where these faults are, whether they can produce earthquakes, and what type of earthquakes they can host. Here we present field geological data from the Beaufort Range fault (BRF) on Vancouver Island that provide the first evidence that the BRF has hosted recent earthquakes. Newly available, high-resolution, topographic data show many scarps, or vertical offsets of the ground surface produced in past earthquakes, along a >35-km-long zone. Surveys of landforms that have been offset by the BRF show both vertical and horizontal offsets along a near-vertical fault. The nearby M 7.3 1946 Vancouver Island earthquake had similar vertical and horizontal motion along a near-vertical fault, suggesting that the earthquake might have happened on the BRF. Our data show there have been at least 3 large earthquakes on the BRF since ~15,000 years ago, the most recent <4,000 years ago. We observe offsets that suggest these earthquakes had magnitudes between ~6.5 and 7.5. Future similar earthquakes could cause shaking damage to many nearby communities, including the cities of Port Alberni and Nanaimo, and nearby hydroelectric facilities.

Production Editor: Christie Rowe and Alice Gabriel
Handling Editor: Jason Padgett
Copy & Layout Editor: Anna Ledeczi

Signed reviewer(s): Stephen Angster, Ian Pierce, and Alan Nelson

Received: 8 December 2023
Accepted: 21 July 2025
Published: 13 August 2025

1 Introduction

Recent advances in our understanding of subduction dynamics show that forearc deformation and stress states vary in both space and time, and can favor extension, strike-slip, or compressional regimes (e.g., Loveless et al., 2010; Toda et al., 2011; Hardebeck and Okada, 2018; Regalla et al., 2017; Herman and Govers, 2020). Particularly in subduction zones like Cascadia, where upper-plate seismicity is sparse, our ability to reconstruct forearc stress and strain states, to identify active faults, and to assess potential hazards using decadal-scale instrumental data alone is limited. This challenge can be addressed through the integration of millennial-scale (geologic) with the decadal-scale (instrumental) earthquake records. Paleoseismic, stratigraphic, and geomorphic data that record deformation over millennial timescales are therefore critical in assessing the longevity and evolution of forearc stress and strain states, the history of the upper plate during megathrust seismic cycles (e.g., Regalla et al., 2017; Herman and Govers, 2020), and the potential hazard of forearc faults (e.g., Thenhaus and Campbell, 2002; Morell et al., 2020; Benavente et al., 2022).

Several lines of evidence suggest that forearc stress states and strain histories in the northern Cascadia fore-

*Corresponding author, elynch@usgs.gov; Now at: U.S. Geological Survey Geologic Hazards Science Center, Golden, CO, USA

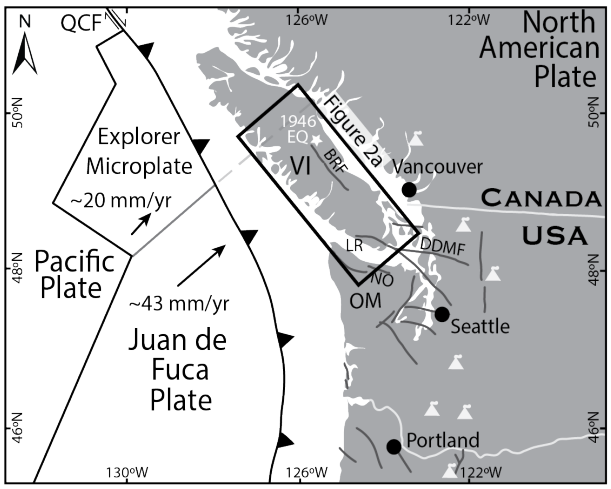

Figure 1 Regional tectonic setting showing the location of the Beaufort Range fault (BRF) and other active faults in the Cascadia forearc of Canada and the USA. Juan de Fuca–North America plate convergence vector after Kreemer et al. (2014). Explorer–North America plate convergence vector after Gao et al. (2017). Active faults in USA after U.S. Geological Survey (2018), Leech River fault after Morell et al. (2017), volcanoes (light gray triangles) after American Geosciences Institute (2003), 1946 Vancouver Island earthquake epicenter (white star) after Rogers and Hasegawa (1978). Black box shows location of Figure 2a. DDMF—Darrington-Devils Mountain fault; LR—Leech River fault; NO—North Olympic fault zone; OM–Olympic Mountains; QCF—Queen Charlotte fault; VI—Vancouver Island.

arc of Vancouver Island (Figure 1) are not adequately characterized by decadal-scale instrumental records alone. First, geodetic displacements in the northern Cascadia forearc are primarily related to transient locking on the megathrust, which obscures records of upper-plate strain (e.g., Li et al., 2018b; Mazzotti et al., 2002). Second, studies have demonstrated that permanent forearc deformation may not be completely caused by stresses imposed from interseismic megathrust locking (Delano et al., 2017; Herman and Govers, 2020; Duckworth et al., 2021; Harrichhausen et al., 2024). Third, upper-plate seismicity is sparse and infrequent in central Vancouver Island, with rates of $<$100 events recorded per year (Balfour et al., 2011; Mulder, 1995). These rates are far lower than in southern Vancouver Island, making kinematic stress inversions challenging. Finally, focal mechanisms of small earthquakes sourced in the northern Cascadia forearc show nearly equal amounts of strike-slip and normal faulting on central Vancouver Island and near-equal horizontal and vertical stress magnitudes (Wang et al., 1995; Balfour et al., 2011; Li et al., 2018a). These data suggest the current forearc stress state is transient and may fluctuate between compressive, strike-slip, and normal faulting conditions over 100–1000-yr timescales throughout one or more megathrust cycles (Wang et al., 1995).

Despite the relatively minimal rates of seismic and geodetic strain, the forearc crust of northern Cascadia hosts faults capable of seismogenic slip, as inferred by the occurrence of the M 7.3 1946 Vancouver Island earthquake, the largest onshore historic earthquake in Canada (Figure 1; Rogers and Hasegawa, 1978; Rogers, 1979; Lamontagne et al., 2018). The 1946 earthquake epicenter was located near the northern tip of the Beaufort Range fault (Figures 1 and 2), and focal mechanism solutions suggest it occurred along a high-angle, upper-plate fault that accommodated right-lateral and extensional slip (Rogers and Hasegawa, 1978; Rogers, 1979). The 1946 earthquake caused moderate damage to nearby population centers, including Port Alberni, Comox, and Campbell River on Vancouver Island, and Powell River on the BC Mainland (Hodgson, 1946; Mathews, 1979; Clague, 1996). Yet, no surface ruptures were documented in the dense forest, the fault that ruptured in the 1946 earthquake remains unknown, and it is unclear if transtensional earthquakes like the 1946 earthquake typify the region.

Here, we present the first field-based evidence of post-glacial (Late Pleistocene to Holocene) surface-rupturing earthquakes along the Beaufort Range fault (BRF), which has been proposed as a possible source of the 1946 Vancouver Island earthquake (Rogers and Hasegawa, 1978; Rogers, 1979). We conducted extensive field mapping and surveying of fault scarps, Quaternary deposits, and incised channels along $>$20 km of the fault that show multiple episodes of lateral and vertical displacement. These data demonstrate that the BRF has accommodated right-lateral-oblique slip at rates of $\sim$0.5–2 mm/yr since $\sim$14 ka, placing the BRF among the fastest of any known faults in the northern Cascadia forearc. These data indicate that the northern Cascadia forearc is accruing permanent, transtensional strain over millennial timescales. Furthermore, the similarities between the near-surface geometry and kinematics of the BRF and focal mechanism solutions for the 1946 earthquake suggest the BRF is a viable candidate fault to have hosted this event.

2 Geologic Setting

The BRF is located in the northern forearc of the Cascadia subduction zone where the Juan de Fuca plate subducts under the North America plate at a rate of $\sim$43 mm/yr (Figure 1; DeMets et al., 2010; Kreemer et al., 2014). The BRF is located along the western flank of the Beaufort Range, a $\sim$1600-m-tall, $\sim$70-km-long, asymmetric, glacially-scoured mountain range on central Vancouver Island positioned $\sim$60 km south of the projected northern terminus of the Juan de Fuca slab (Figure 1; Figure 2b). Active faults (i.e., those that have ruptured in the Late Pleistocene to Holocene) that accommodate forearc strain are recognized along most of the Cascadia subduction zone in the United States and southernmost Vancouver Island, Canada (e.g., Figure 1). These faults have each hosted at least one to five earthquakes in the late Quaternary, and have slip rate estimates ranging from $\sim$0.1 to $\sim$1.5 mm/yr. However, no active faults have been previously identified in the northernmost $\sim$300 km of the Cascadia forearc on Vancouver Island.

Two major geologic events have shaped the topography and geology of the study area. The first is an

Eocene contractional event that formed the Cowichan fold and thrust system during terrane accretion (England, 1990; England and Calon, 1991; England et al., 1997). The northernmost thrust fault of the Cowichan fold and thrust system, previously named the Beaufort Range fault, is mapped for >40 km along the southwestern side of the Beaufort Range near its base (Figure 2a; Cui et al., 2017; England and Calon, 1991). In this paper, we refer to this thrust fault as the "Eocene bedrock thrust fault" to distinguish it from the active fault that we document herein (the BRF); we discuss the relationship between bedrock faulting and Quaternary fault scarps in Section 8.5.

The NE-dipping Eocene bedrock thrust fault places Late Triassic Karmutsen Formation (Fm.) basalts over Cretaceous Nanaimo Group sediments, such that the peaks of the Beaufort Range are underlain by basalt and the adjacent Alberni Valley is underlain by sedimentary rocks (Figures 2a, S1; Muller and Carson, 1969). In the hanging wall of the Eocene bedrock thrust fault, basalt flow tops in the Karmutsen Fm. are generally planar and dip gently (<20°) toward the SW (Figure 2a). Geologic mapping, balanced cross sections, and seismic reflection profiles suggest the bedrock thrust fault dips NE, at 45° to ~60° (Yorath et al., 1985a,b; Clowes et al., 1987). Low-temperature thermochronology data indicate that uplift and exhumation of rocks in the Cowichan fold and thrust system occurred at ~40–50 Ma (England, 1990; England and Calon, 1991; England et al., 1997). No post-Eocene thrust sense deformation has been documented along the bedrock fault (Figures 2a, S7; Muller and Carson, 1969; Cui et al., 2017).

The second major event that shaped the geology of the study area was scouring and sedimentation during Late Pleistocene glacial episodes. Existing maps document till, colluvial, and alluvial deposits that extend to an elevation of ~300 m along the range front (Fyles, 1963). While no units in the study area have been previously dated directly, glacial deposits in the Alberni Valley have been correlated to the last glacial maximum at ~13.6–11 ka, based on ages from marine shells, peat, and wood in glaciomarine deposits in the Strait of Juan de Fuca and along the eastern coast of Vancouver Island (e.g., Clague et al., 1980; Easterbrook, 1992). These units have been correlated to two major episodes of glaciation. The region was first inundated by the south-southwestward flowing Cordilleran continental ice sheet during the Fraser stage glaciation (~25->12 ka; Fyles, 1963; Alley and Chatwin, 1979; Clague and Ward, 2011). Then, during the retreat of the ice sheet, the Alberni Valley was occupied by a southeastward-flowing valley glacier that produced streamlined landforms and associated glacial deposits that trend subparallel to the valley bottom (Mosher and Hewitt, 2004; Easterbrook, 1992; Clague and James, 2002).

3 Approach and methods

We undertook a multi-stage approach to identify fault-related deformation (e.g., fault scarps) in dateable Quaternary sediments and to characterize the slip history of any active faults we documented (e.g., Sieh, 1978; McCalpin, 1996). First, because the study area contains dense temperate rainforest and thick soils that limit exposure and accessibility, we began with regional-scale mapping using lidar and air photos. Of critical importance were new lidar Digital Elevation Models (DEMs) along the BRF generated from newly available airborne lidar point clouds (see Data and code availability statement for lidar information). We used the DEMs to identify glacial and post-glacial landforms and map potential fault scarps, though in most instances, the lidar resolution was insufficient to measure offset of geomorphic features. Second, we conducted field work to determine stratigraphy and stratigraphic relationships among the Quaternary units, to complete detailed lithologic descriptions of those units, and to collect samples for radiocarbon dating where possible (results are described and illustrated in Section 4). Third, we visited as many potential fault scarp outcrops as were physically accessible to map them in detail, evaluate if scarps were most likely produced by tectonic or non-tectonic processes, and to document evidence of tectonic displacement of Quaternary units (methods and results described in Section 5). Fourth, to evaluate whether any Quaternary scarps reoccupy fault planes associated with Eocene bedrock thrust faults and shear zones, we mapped bedrock lithology and faulting in the field, along the entire Beaufort Range, wherever accessible (see Section 6). Fifth, we conducted topographic surveys across tectonic scarps to quantify the magnitude and direction of slip and to infer slip rates where radiometric ages were available (Section 7). Finally, we used our results to infer the post-glacial slip history of the BRF and to consider whether our data are consistent with the 1946 earthquake having occurred along this fault (Section 8).

4 Mapping of Quaternary stratigraphy and landforms

4.1 Lidar-assisted and field mapping of surficial features

We completed regional-scale mapping of an ~100-km-long swath of the western side of the Beaufort Range (Figures 2, S1), in order to identify Quaternary units or landforms that may be displaced by active faults, and to identify areas for focused field investigation. Beginning with lidar data and air photos, we examined surface topography, roughness, morphology, and inset and burial relationships, and correlated our observations, where possible, to the existing Quaternary units mapped by Fyles (1963). We then took our initial mapping results into the field to confirm stratigraphic relationships, and to describe ice-contact units, paraglacial units, and post-glacial lithological units in detail (Figure 3c).

Within our regional-scale map, we chose two areas for more detailed study and field mapping at 1:3000, because they had high densities of potential fault scarps, contained multiple generations of Quaternary deposits, and had landforms that were particularly well preserved (Sites 1 and 2, Figure 3a-b). Detrital char-

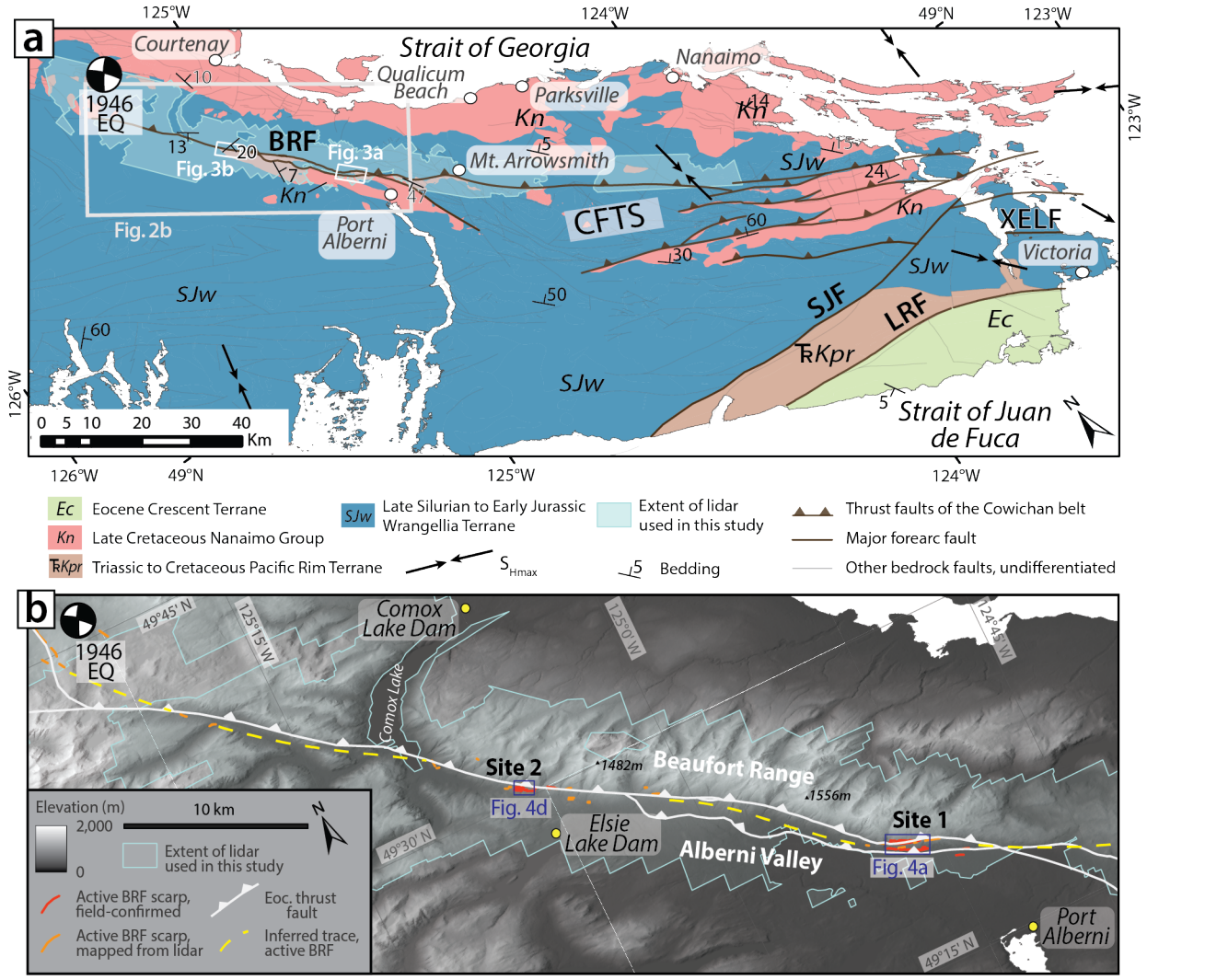

Figure 2 Geologic and geomorphic setting of the Beaufort Range fault. **a:** Simplified geologic map of southern Vancouver Island showing major basement units, thrust faults of the Cowichan fold and thrust system (CFTS), and other forearc faults. The epicenter of the 1946 M 7.3 Vancouver Island earthquake is shown by the focal mechanism (Rogers and Hasegawa, 1978). Maximum horizontal stress directions determined from crustal seismicity after Balfour et al. (2011). Bedding strike and dip simplified from Muller and Carson (1969); England (1990); Massey et al. (1991) and this study. Bedrock geology and faults after the British Columbia Geological Survey compilation by Cui et al. (2017); XELF fault trace after Harrichhausen et al. (2023a). BRF—Beaufort Range fault. LRF—Leech River fault. SJF—San Juan fault. XELF—XEOLXELEK-Elk Lake fault. Detailed mapping at Sites 1 and 2 (small white boxes) is shown on Figure 3 and Supplemental Figure S1. White box shows the location of panel b. **b:** Hillshaded Canadian Digital Elevation Model (Natural Resources Canada, 2013) showing the topography of the Beaufort Range and Alberni Valley, the locations of hydroelectric dams, the trace of the Eocene bedrock Beaufort Range thrust fault, and our interpreted, simplified, trace of the active BRF inferred based on the locations of mapped scarps. Unannotated DEMs of Sites 1 and 2 (blue boxes) are shown in Figure 4.

coal samples were collected from natural and anthropogenic exposures of Quaternary deposits where possible, which yielded radiocarbon ages for three units (Figure 3c, see Supplemental Text S2 for full details of radiocarbon methods).

4.2 Quaternary units, ages, and landforms

4.2.1 Ice-contact glacial deposits and landforms

Ice-contact glacial units are the oldest and stratigraphically lowest Quaternary units and landforms mapped in the study area. At Site 1, these include till (Qt), kame deposits and terraces (Qk), and hummocky moraine (Qhm; Figures 3a, S2; Table S1). The till (Qt) is a very indurated, matrix-supported diamict up to 40 m thick, containing both locally derived and exotic clasts. Qt mantles bedrock along the southwestern flank of the Beaufort Range mountain front at elevations >150–400 m. Qt is the predominant unit exposed at Site 2, surrounding bedrock erosional remnants and underlying post-glacial units described below. Kame deposits (Qk) are indurated, poorly to moderately sorted, stratified sands and gravels that occur near the base of the range. Kame deposits underlie a series of five evenly spaced, flat-topped terrace treads with steep risers, at 150–300 meters above sea level (masl; <150 m above the valley floor, Figure 3a). Hummocky moraine (Qhm) is present on the valley floor at eleva-

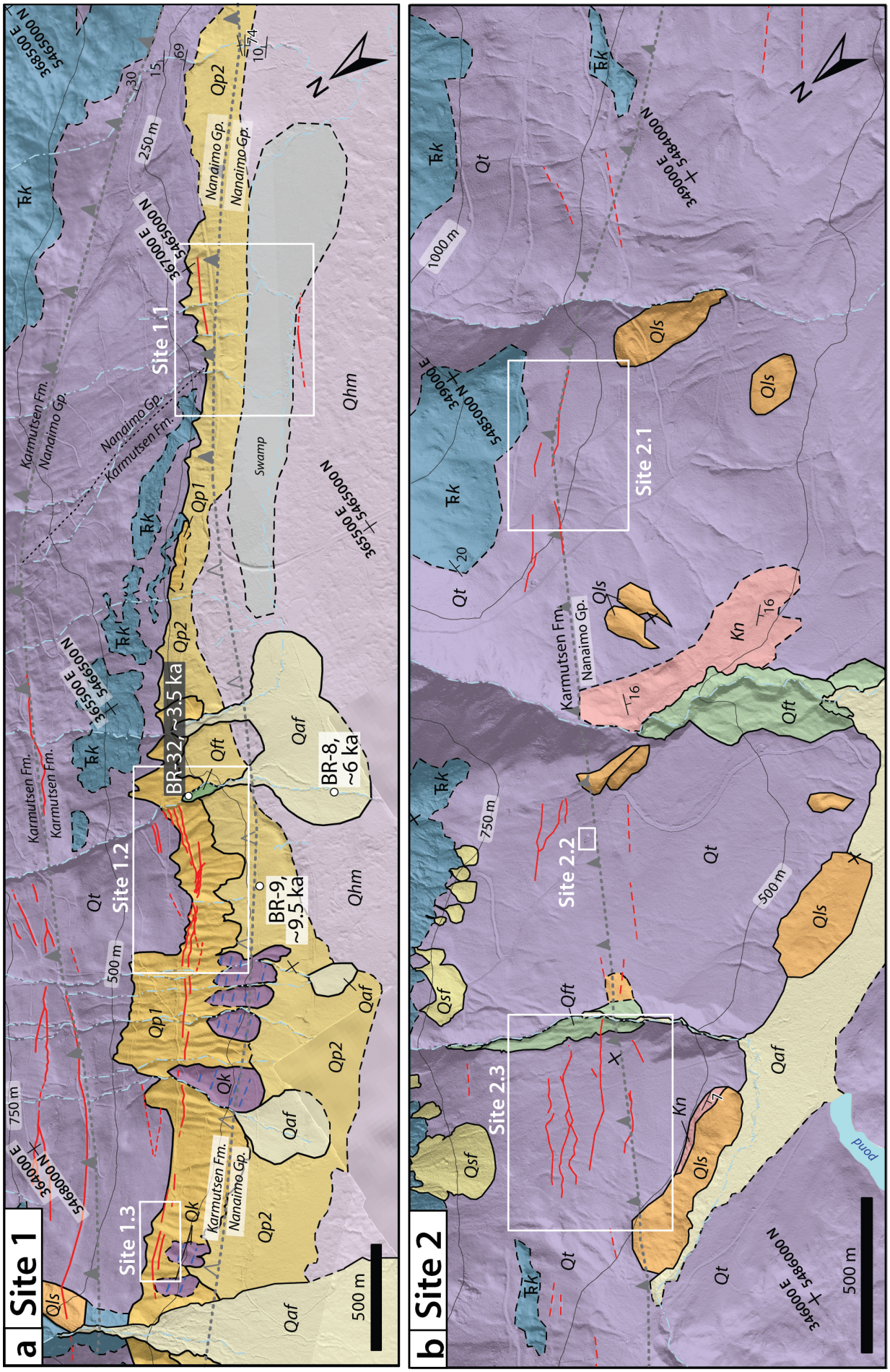
a Site 1
Site 1.1
Site 1.2
Site 1.3
BR-32, ~3.5 ka
BR-8, ~6 ka
BR-9, ~9.5 ka
Karmutsen Fm.
Nanaimo Gp.
Qp1
Qp2
Qaf
Qft
Qhm
Qls
Qk
Trk
Swamp
500 m
750 m
250 m
b Site 2
Site 2.1
Site 2.2
Site 2.3
Qt
Qsf
Kn
pond
1000 m
500 m
750 m
N

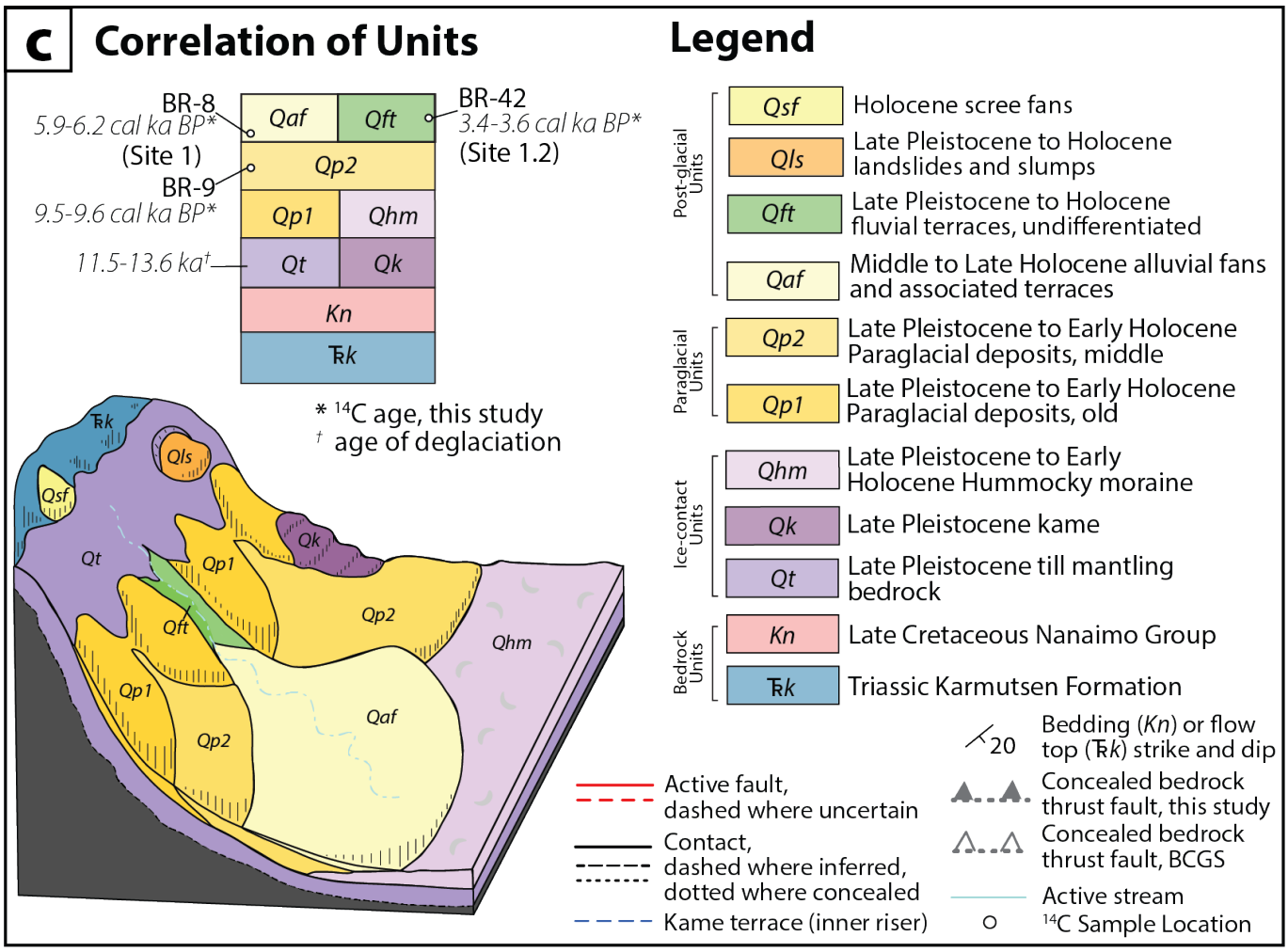

Figure 3 Bedrock and surficial geology of portions of the BRF (See locations in Figure 2a). Mapping is overlain on a composite hillshaded DEM compiled from two bare-earth lidar DEMs gridded to 0.5 m and to 2 m, and from 30 m SRTM DEM (JPL, 2013). Radiocarbon ages are reported in Table 1. Bedrock fault locations compiled from new field mapping and existing mapping by the British Columbia Geological Survey (BCGS; Cui et al., 2017); strikes and dips from this study. White boxes outlining Sites 1.1–2.3 correspond to locations shown in Figures 5, 6, S7 and S9. Map of Site 1, along the southern portion of the BRF, is shown in panel a, and map of Site 2, along the northern portion of the BRF, is shown in panel b. Panels a and b on the preceding page. Fault scarps (red lines) occur at the base of the Beaufort Range and along the rangefront up to 1000 m above the valley floor. Mapped scarps occur in both the hanging wall and footwall of the bedrock BRF. Fault scarps offset multiple ages of glacial (Qt), paraglacial (Qp1, Qp2), and modern deposits (Qls, Qft, Qaf). **c:** Correlation of units and legend for geologic maps in panels a and b. For full unit descriptions, see Table S1. Charcoal samples in these deposits yield ages of ~9600–3400 cal yr BP (Table 1).

tions of <150 masl. The ice-contact deposits did not contain identifiable charcoal and could not be dated directly (Table 1). We interpret Qt, Qk, and Qhm to correlate with the last deglaciation (regionally dated to ~13.6–11.5 ka; Halsted, 1968; Alley and Chatwin, 1979; Blaise et al., 1990; Clague, 1994). We acknowledge the possibility that deposits associated with prior glacial periods may be present in the study area.

4.2.2 Paraglacial deposits and landforms

At Site 1, the ice-contact glacial tills are overlain by two generations of paraglacial deposits, Qp1 and Qp2. Qp1 consists of indurated, clast-supported, poorly sorted, stratified sands and gravels. Qp1 deposits occur as cone-shaped landforms whose noses merge into Qt at higher elevations and whose toes are buried by Qp2 at the foot of the range. Qp2 has a similar composition to Qp1 and consists of thinly-bedded, clast-supported, stratified sands and gravels with occasional coarse sand lenses. Qp2 is distinguishable from Qp1 based on inset and burial relationships and its position at lower elevations. We interpret Qp1 and Qp2 to have formed during a period of rapid landscape change during and immediately following deglaciation (Figures 3c, S2; Table S1; e.g., Ballantyne, 2002).

We collected one charcoal sample, BR-9, from a stratified fan deposit ~30 cm below the surface of Qp2, in a roadcut exposure ~250 m SW of the fault scarps at Site 1 (Figures 4, 3, S3). Sample BR-9 yielded an age of ~9.5 cal ka BP (Table 1), which is consistent with the older estimated age of the Late Pleistocene glacial deposits (Qt, Qk, and Qhm) of ~13.6–11.5 ka BP. The ~9.5 cal ka age is also consistent with the timescales of paraglacial debris

cone formation documented in recently deglaciated terrains that suggest paraglacial debris cones and fans form in the first 100s-1000s of years following deglaciation (Ryder, 1971; Ballantyne and Benn, 1996; Ballantyne, 2002).

4.2.3 Post-glacial units and landforms

The youngest units include post-glacial landslides (Qls), scree fans (Qsf), alluvial fans (Qaf), and fluvial terraces (Qft) that either bury or are inset into the glacial and paraglacial deposits (Figure 3, Table S1; Figure S2). Mapped landslides (Qls) are hummocky deposits associated with curvilinear headscarps and oversteepened toes and have widths of 50–600 m. Scree fans (Qsf) are small (30–250 m across) fan-shaped deposits with rough surfaces that contain cobble- to boulder-sized bedrock clasts. Qsf occurs at the bases of mapped bedrock exposures at elevations of ∼750 masl. Alluvial fan deposits (Qaf) are defined as a series of broad, convex, gently-sloping fans headed in active or recently active channels (Figure 3). Alluvial fans consist of poorly to moderately sorted, clast-supported, stratified deposits containing silt, sand, pebbles, and boulders, with occasional clast imbrication and cross-bedding (Table S1). Qaf deposits are mapped at the base of the range front and bury portions of Qp2, Qt, and Qhm.

At two locations within Site 2 and one within Site 1, Qaf fan noses merge into deeply incised streams (by ∼1–15 m) that are flanked by a series of up to five fluvial terraces (Qft, Figure 3b). Fluvial terrace treads are 20–130 m wide, slope gently downstream, and have risers up to 5–10 m high. The deposits that underlie the terraces are moderately to well-sorted, clast-supported sediments with sub-horizontally stratified interbeds of rounded cobbles, boulders, and pebbles. At Site 2, Qft terraces are inset into till-mantled bedrock and are, in turn, incised by channels feeding Qaf alluvial fans (Figure 3b), a stratigraphic relationship that shows that at Site 2, Qft terraces are older than Qaf. In contrast, at Site 1, Qft appears to grade into the channels that feed Qaf, indicating that Qft terraces are younger than at Site 2 and are instead correlative to upper portions of Qaf or the channels inset into Qaf (Figure 3a).

Units Qaf and Qft yielded dateable charcoal fragments. Sample BR-8 was collected from a stratified, clast-supported sand lens within interbedded sands and gravels in Qaf, ∼0.75 m below the top of the deposit located ∼500 m SW of fault scarps at Site 1 (Figures 3, 4, S3). Qft yielded a charcoal sample, BR-42, that was sieved from a bulk sediment sample collected from a stream cut exposure of stratified pebbles and cobbles, located <10 m downhill from mapped fault strand Ee (Figures 3a, 4, S3). Samples BR-8 and BR-42 are younger than the age of BR-9 from paraglacial deposit Qp2 (∼9.5 cal ka BP), suggesting that Qaf is older than Qft at Site 1.

4.2.4 Abandoned channels

Paraglacial unit Qp1 is incised by a series of abandoned, well-preserved paleochannels at Sites 1 and 2 that are currently disconnected from the modern

Table 1 Radiocarbon sample data at Site 1.2 (see Figure 3 for locations).

Unit[a]	Coordinates[b]	Sample Name	Sample Type	Dated Material	UCIAMS ID[c]	Fraction Modern	$D^{14}C$ (‰)	Radiocarbon Age[d] (years BP, 1 σ)	Calibrated (cal yr BP)	Age[e]
Qft	364944 E, 5466432 N	BR-42	Bulk sediment	Charcoal *(single piece)*	215250	0.6658 ± 0.0013	-334.2 ± 1.3	3265 ± 20	3560–3400	
Qaf	364561 E, 5465854 N	BR-8	Macro charcoal	Charcoal *(single piece, ∼1 cm)*	215248	0.5185 ± 0.0010	-481.5 ± 1.0	5275 ± 20	6180–5940	
Qp2	364400 E, 5466402 N	BR-9	Bulk sediment	Charcoal *(composite of three ∼mm-size pieces)*	215249	0.3428 ± 0.0008	-657.2 ± 0.8	8600 ± 20	9600–9520	

[a] See Figure 3 and Table S1
[b] NAD83 UTM Zone 10
[c] Samples were prepared at PaleoTek Services. Sample preparation backgrounds have been subtracted, based on measurements of ^{14}C-free wood. These samples were treated with acid-base-acid (1N HCl and 1N NaOH, 75°C) prior to combustion. Samples were processed at the UC Irvine Keck AMS facility.
[d] All results have been corrected for isotopic fractionation according to the conventions of Stuiver and Polach (1977), with $d^{13}C$ values measured on prepared graphite using the AMS spectrometer. These can differ from $d^{13}C$ of the original material, and are not shown.
[e] Radiocarbon ages calibrated using INTCAL20 (Reimer et al., 2020) and OxCal v. 4.4 (Bronk Ramsey, 2021). Range reported represents unmodeled 95% confidence interval as calculated by OxCal.

stream network. The paleochannels at Site 1 incise till and colluvium-mantled hillslopes, are typically ~1–4 m deep, have V-shaped cross-sections, and are separated by interfluves with linear ridges and steep flanks (Figures 3 and 4). These paleochannels incise Qp1, and merge into the heads of Qp2 deposits, suggesting that they were active at the time of deposition of Qp2, but no longer accommodate significant discharge. We interpret the paleochannels at Site 1 to have formed as the result of fluvial and debris flow scouring and filling associated with the deposition of Qp2. At Site 2, offset paleochannels have broad cross-sectional morphologies and are moderately incised into hummocky, till-mantled hillslopes (Figures 3 and 4). The paleochannels at Site 2 do not clearly merge into other mapped deposits but appear to be cross-cut by younger landslides at the foot of the range.

5 Quaternary scarps

We used lidar DEMs, field observations, satellite imagery (Google Earth Pro, 2016), and historical air photos (British Columbia provincial government, 1947 and 1952) to evaluate the geometry and context of the topography and identify potential fault scarps. We applied our scarp mapping approach within a 100-km-long swath of the western Beaufort Range between the epicenter of the 1946 Vancouver Island earthquake and Mt. Arrowsmith (Figure 2). We identified linear and curvilinear features that are continuous for >50–100 m and appear to cut across topography and/or Quaternary landforms (e.g., abandoned channels; Figure 4b-c). We then examined each feature to rule out candidate fault scarps that likely formed by non-tectonic processes, such as anthropogenic disturbances, glacial or gravitational processes, or differential erosion of bedrock.

Landforms of non-tectonic origin include logging roads, landslide scars, sackungen, glacially striated, scoured, and plucked surfaces, and scarp-like landforms formed by differential erosion (Figure S4). Logging roads typically exhibit a flat base with an oversteepening of the lateral flanks. Landslide head scars or "toes" are typically curvilinear and often associated with hummocky deposits and disrupted topography. Scarps formed by sackungen typically occur parallel to topographic contours near the top of the range (elevations of >1300 m) in parallel linear sets <500 m long (e.g., McCalpin, 1990). Neither landslide head scars nor sackungen typically extend across multiple hillsides or drainages. Glacially streamlined deposits and glacially-plucked surfaces tend to have an asymmetry axis parallel to the ice transport direction (~120° azimuth), and the elevation of crests of glacial lineaments typically decreases in that same direction. Scarp-like landforms formed by differential erosion are co-located with steeply dipping bedding planes or changes in lithologic strength across Karmutsen Fm. flow tops.

Scarps that we determined to be produced by tectonic processes, in comparison, are ~100–2000 m long, and occur in en echelon or parallel sets with spacings of 5–100 m. They occur at elevations of ≤500 m above the valley floor and do not occur in the upper ~700 m of the range (above ~800 m). Individual scarps have trends of ~270–300°, cross topographic contours, and have asymmetric cross-sectional geometries. Tectonic scarps cross-cut multiple generations of Quaternary deposits and landforms, and produce vertical separation of the hillside.

In total, we identified 127 tectonically produced scarps within the 100-km-long swath we examined using a combination of field and lidar-based observations (Figure S1). First, all scarps were carefully evaluated on lidar DEMs to assess the criteria listed above to interpret tectonic vs. non-tectonic scarps. Then, we visited all scarps that were physically accessible in the field to use additional field observations of geomorphic form and context to assess if they were best interpreted as being of tectonic or non-tectonic origin. Of the entire set of scarps identified from lidar DEMs, we visited and mapped 79 as tectonic in the field, spanning a total distance of ~35 km. We then further focused our scarp mapping, evaluations, and descriptions in the two focus areas at Sites 1 and 2.

At Site 1, we identified a branching set of 3–5 en echelon scarps (e.g., strands F, G, Ew on Figures 5d, 7f). Scarp heights on individual strands range from 0.5 m to 6 m. The steepest and tallest scarps are 4–6 m high and have faces near the angle of repose (32° for strand Ew at Site 1.2; Figures 5, 7b,f,g). Other scarps exhibit a more moderate, 23°-dipping scarp face, such as Strand D at Site 1.2 (Figure 7e). Most of the mapped scarps (~70%) have asymmetrical cross-sectional morphologies with steep, uphill-facing scarps, while a smaller fraction are preserved as flat, degraded, topographic features embedded in the high-gradient hillslopes (Sites 1.1–2.3; Figures 4, S4d). Every abandoned channel and preserved interfluve that crosses mapped scarps is truncated and displaced laterally by at least ~0.5–2 m (Figure 7a-c).

At Site 2, scarps occur as parallel or anastomosing sets of 3–6 strands (Figure 6). The steepness and morphology of scarp faces vary along strike and among strands. Scarp heights range from 1 to 3 m, with faces near the angle of repose (~45° for strand U at Site 2.3; Figure 6 and S5), and some are large and steep enough to have effectively ponded large boulders sourced from uphill (Figure S5). Scarp facing directions vary locally over short distances, but about two-thirds of the scarps (n=101) face uphill to the NE. Three stream channels are systematically right-laterally sheared by several meters across 3–5 fault strands (Figure 6).

The scarp geometries, morphologies, and map patterns we observed are most consistent with those that form along faults in transtensional tectonic systems. Based on their 'V' patterns as they intersect topography, these scarps appear to be the product of slip along a set of steeply-dipping (~70°), ESE-WNW trending (~287°) faults. Field observations show consistent vertical and lateral offsets of geomorphic piercing lines across scarps at multiple independent sites, regardless of local topographic slopes, elevations above the valley floor, or bedrock versus Quaternary substrate. Mapped scarps clearly project into adjacent scarps across gaps and stepovers, occur in en echelon and parallel arrays,

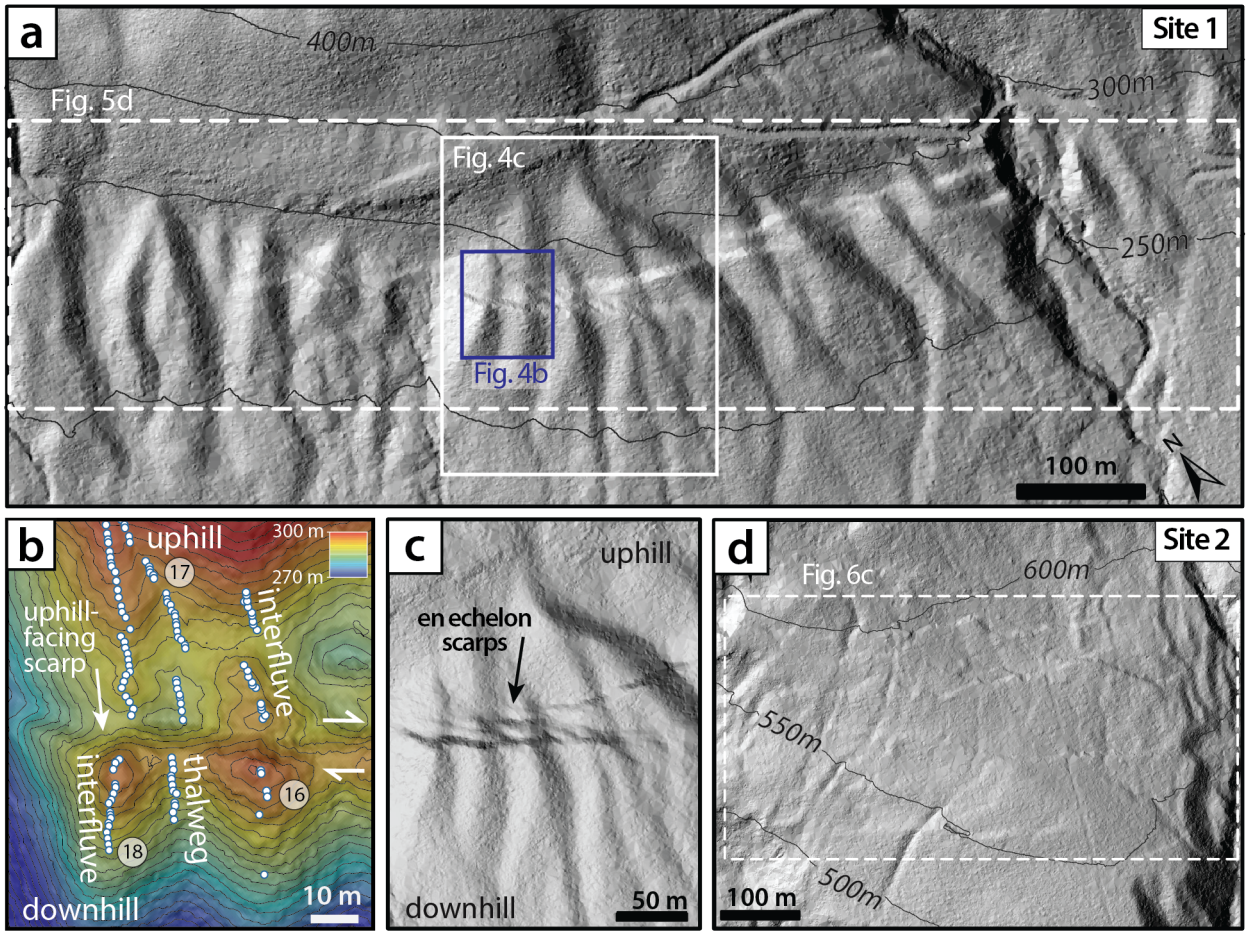

Figure 4 Examples of tectonic fault scarps visible in hillshaded (315° azimuth, 45° altitude) bare-earth lidar DEMs. **a:** Unannotated DEM of Site 1 showing a network of en echelon ~1- to 6-m-high fault scarps offsetting a series of abandoned channels and interfluves (see Figure 2b for location). **b:** Example of an uphill facing scarp developed on a till-mantled hillside. The scarp offsets a channel thalweg and adjacent interfluve crests both vertically (downhill-side-up) and right-laterally. White dots show locations of individual survey points, which may not match contours perfectly due to lidar resolution and projection. Contour interval is 1 m. **c:** Example of en echelon array of scarps at Site 1. **d:** Unannotated DEM of Site 2 showing a network of right-laterally sheared channels (see Figure 2b for location). Examples of non-tectonic landforms are presented in Supporting Information Figure S4.

and span several tens of kilometers of strike length. Similar geometries are common in documented strike-slip fault systems and pull-apart basins, particularly those with relatively low cumulative offset (e.g., Wesnousky, 1988; Hatem et al., 2017; van Wijk et al., 2017).

6 Bedrock mapping

We mapped bedrock lithology and faulting along the entire Eocene bedrock thrust fault from lidar and in the field, with more detailed field efforts at Sites 1 and 2 (Figure 2). We identified the location of the Eocene bedrock thrust fault from direct outcrop exposures of the fault, zones of increased rock damage and deformation, and outcrop positions of differing hanging and footwall units. At each fault contact and damage zone exposure, we measured fault planes, slickenlines, foliation fabrics, and fractures. At locations outside of the fault zone, we measured the strike and dip of basaltic flow tops and bedding. We complemented this field mapping with interpretation of lidar topography in inaccessible areas, or where no outcrop was found. We used bedrock outcrops, and outcrops of the fault zone itself at Sites 1.1 and 2.1, to refine and update the mapping of the location of the Eocene bedrock thrust fault (solid teeth in Figure 3; c.f. Cui et al., 2017).

At Site 1, we mapped two branches of the Eocene bedrock thrust fault (Figure 3). The upper thrust fault branch places Triassic Karmutsen Fm. over Late Cretaceous Nanaimo Group (Gp.) sedimentary rocks east and north of Site 1.1 and over Karmutsen basalts west of Site 1.1. The lower thrust branch places Karmutsen Fm. and Nanaimo Gp. rocks over the Nanaimo Gp. Bedrock fault exposures throughout Site 1 show that the hanging wall of the upper thrust fault contains heavily fractured basalt, with an increase in fracture density, alteration, and foliated fabric intensity toward the fault core. Fault and shear planes exposed at these sites either dip steeply to moderately toward the SW or gently toward the NE (Figure S6). The footwalls of both thrust branches contain tight footwall synclines developed in Nanaimo Gp. sediments. In each footwall syncline, bedding dips change from 10° SW to near vertical over a horizontal distance of ~70 m; we therefore in-

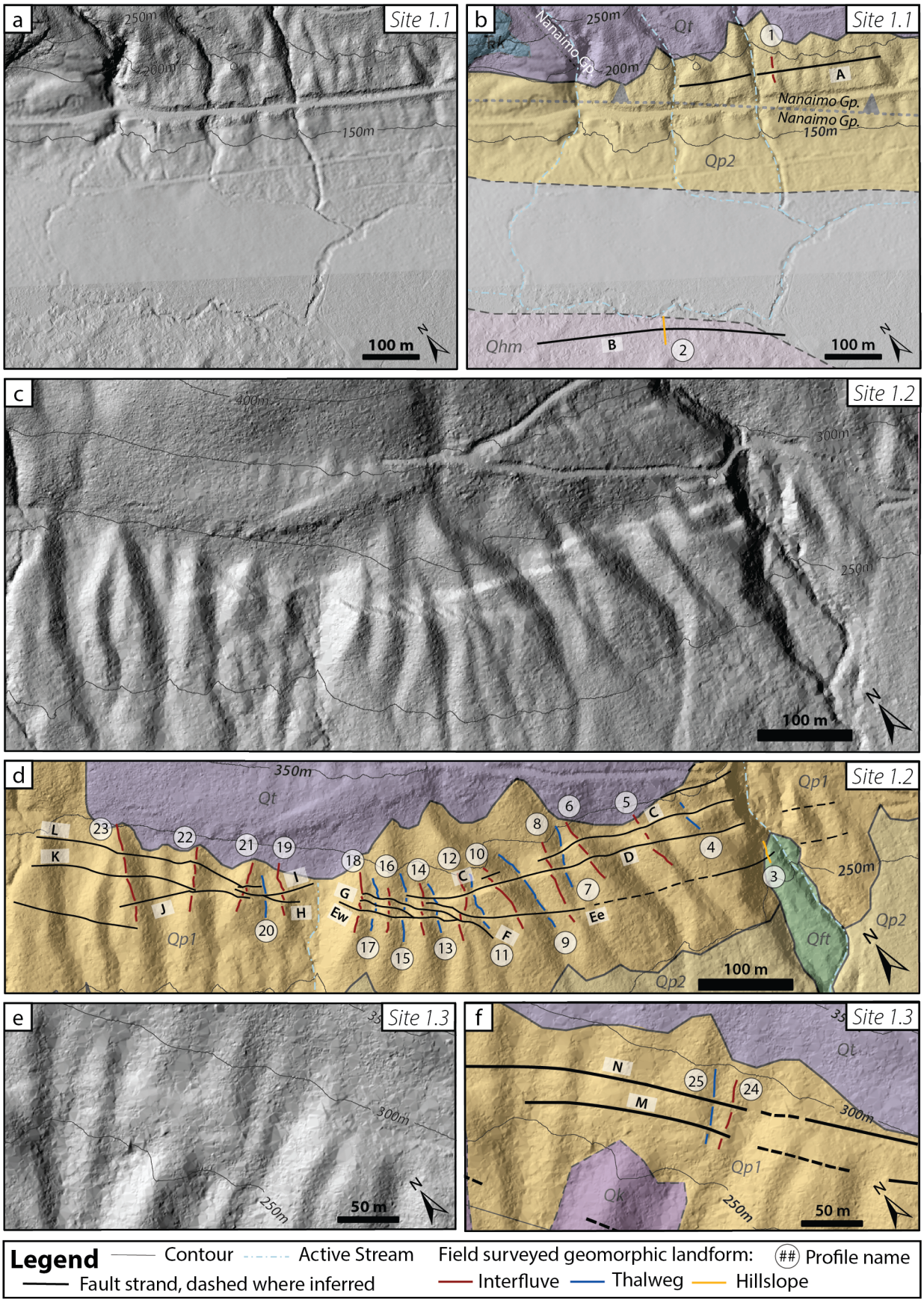

Figure 5 Unannotated hillshaded lidar DEMs of Sites 1.1, 1.2, and 1.3 (a, c, e, respectively), and annotated hillshaded DEMs showing mapped faults (labeled from A to N) and surveyed topographic profiles (numbered from 1 to 25) of Sites 1.1, 1.2, and 1.3 (b, d, f, respectively). See Figure 3 for locations and surficial mapping legend, and Dryad data repository for topographic profile survey data (Lynch et al., 2025).

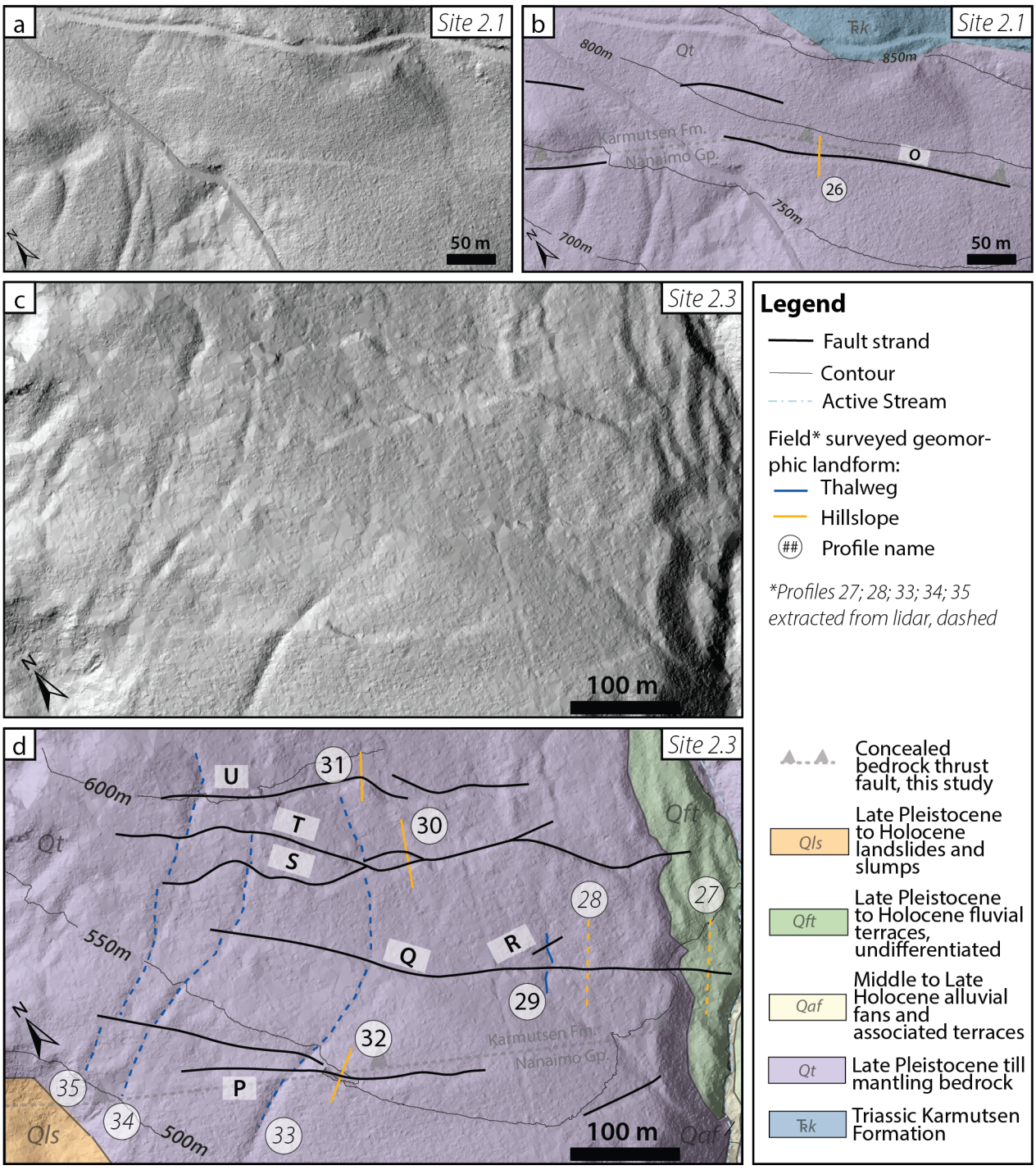

Figure 6 Unannotated hillshaded lidar DEMs of Sites 2.1 and 2.3 (a and c, respectively), and annotated hillshaded DEMs showing mapped faults (labeled from O to U) and topographic profiles (numbered from 26 to 35) of Sites 2.1 and 2.3 (b and d, respectively). See Figure 3 for locations and surficial mapping legend, and Dryad data repository for topographic profile data (Lynch et al., 2025).

terpret the fold axes to be located near each main fault trace. We observe predominantly dip-slip slickenlines at Site 1, primarily on damage zone planes (Figure S6). Karmutsen Fm. basalt flow tops and Nanaimo Gp. bedding in the hanging wall dip gently to the SW (Figures 2b, 3b; Cui et al., 2017). We observe no evidence of folding in the basalt in the hanging wall at Site 1, nor did we find evidence of an anticline in Nanaimo Fm. outcrops in the hanging wall southeast of Site 1 near Mt. Arrowsmith (Figure 2a).

At Site 2, there is one, steeply-dipping bedrock thrust fault strand that places Triassic Karmutsen Fm. basalt over Late Cretaceous Nanaimo Gp. sedimentary rocks (Figures 3b, S6). The Eocene thrust fault contact and damage zone are clearly exposed at Site 2.1. The hanging wall north of the fault contains a damage zone of fractured Karmutsen Fm. basalt, with increasing fracture density within 100 m of the fault core. The main lithologic fault contact consists of a ~30–100 cm gouge zone separating Karmutsen basalt from Nanaimo Gp. conglomerate, surrounded by a series of <10 cm-wide gouge zones in hanging wall basalts, and ~20 cm- to

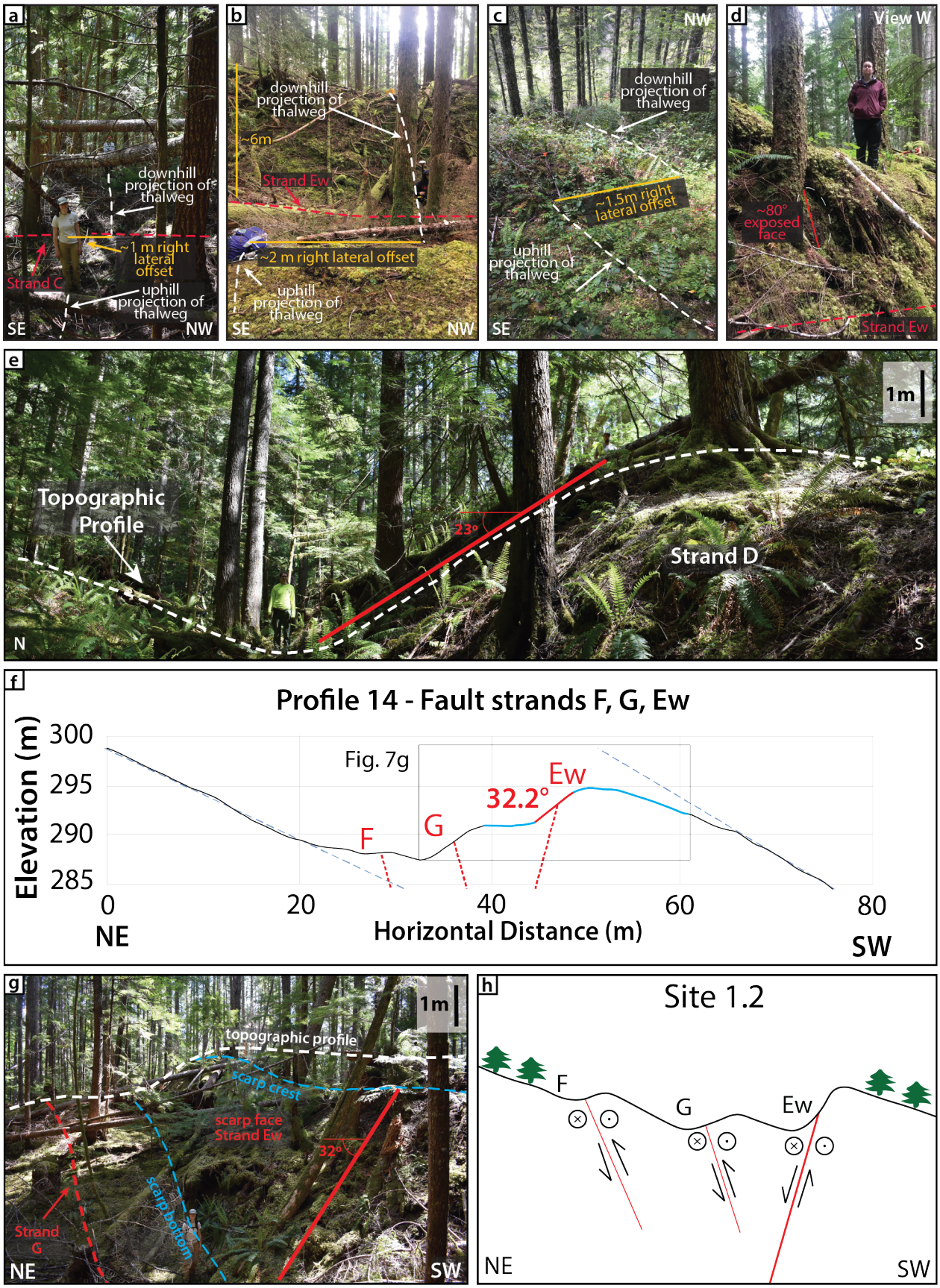
a
downhill projection of thalweg
~1 m right lateral offset
Strand C
uphill projection of thalweg
SE
NW
b
downhill projection of thalweg
~6m
Strand Ew
~2 m right lateral offset
uphill projection of thalweg
SE
NW
c
NW
downhill projection of thalweg
~1.5m right lateral offset
uphill projection of thalweg
SE
d
View W
~80° exposed face
Strand Ew
e
1m
Topographic Profile
23°
Strand D
N
S
f
Profile 14 - Fault strands F, G, Ew
Elevation (m)
300
295
290
285
Fig. 7g
Ew
32.2°
F
G
0
20
40
60
80
NE
Horizontal Distance (m)
SW
g
1m
topographic profile
scarp crest
scarp face Strand Ew
32°
scarp bottom
Strand G
NE
SW
h
Site 1.2
F
G
Ew
NE
SW

Figure 7 *Previous page.* Examples of right-lateral offsets and fault scarps identified along the Beaufort Range fault. **a.** Field photo of vertical and right-lateral displacement of profile 5 at strand C. See Figure 5 for profile location. **b.** Field photo of vertical and right-lateral displacement of profile 17 at strand Ew. See Figure 5 for profile location. **c.** Field photo of vertical and right-lateral displacement of a channel form north of Site 2. **d.** Field photo of an exposed ∼80°-dipping face along strand Ew between profiles 16 and 17. **e.** ∼5-m-high, uphill-facing, moderately steep (∼23°) fault scarp along strand D at Site 1.2 (Figures 3a, 5d). **f.** Topographic profile across three scarps at Site 1.2 associated with fault strands F, G, and Ew extracted from bare-earth lidar DEM (Profile 14, Figure 5). Fault dips calculated from surveyed scarp midpoints. Dashed dark blue lines show the projection of the background hillslope toward the scarps. **g.** Photo of the ∼6-m-high, steep, preserved face of Strand Ew shown in the topographic profile in panel f. The uphill-facing fault scarp along strand Ew is ∼32°, much steeper than the scarp face along strand D (panel e). **h.** Cartoon cross-section showing the schematic relationships between sets of sub-parallel and en echelon fault strands, based on observations at Site 1.2. These strands are interpreted to merge at depth in a flower structure consistent with strike-slip faulting.

2-m-wide gouge zones in footwall sedimentary rocks. Bedding in the Nanaimo Fm. is tightly folded into a footwall syncline, dipping 80° S at 15 m from the fault core, shallowing to 30° S at 100 m from the fault core, and sub-horizontal ∼800 m from the fault. At Site 2.2, we observe damage in the Karmutsen basalt, including a population of planes we interpret to be Riedel shears related to a NW-SE-striking, SW-dipping thrust fault plane (Figure S6). We observe slickenlines at Site 2.2, primarily on planes within the damage zone. A subset of main fault planes have slickenlines consistent with right-lateral and dip-slip motion (Figure S6). Here, the bedrock fault zone in outcrop is overlain by an undeformed drape of till (Figure S7). We do not observe any evidence of folding in the Karmutsen Fm. in the hanging wall at Site 2 bedrock exposures.

7 Quantifying fault slip across scarps

7.1 Profile collection and reconstruction methods

We quantified the magnitude and direction of slip across mapped tectonic fault scarps using field-based topographic profiles of offset geomorphic piercing lines. Although lidar DEMs proved instrumental in identifying scarps, these data were of insufficient quality to enable delineation of piercing lines and measurements of displacements with confidence. Dense undergrowth prevented the lidar from reaching true ground, and large trees blocked returns for areas up to 10 m across (Figure S8). Uneven return spacing precluded the use of DEM backslipping techniques to quantify displacements (e.g., LaDiCaoz; Zielke and Arrowsmith, 2012). We therefore collected topographic profiles in the field using Nikon XS and Spectra Precision Focus 6 total stations, and used the data to reconstruct fault slip vectors at Sites 1 and 2. Our methods are described briefly here, but full details of our methods and estimation of uncertainties are provided in the Supporting Information file (Text S3).

Three-dimensional slip vectors can be determined where fault scarps intersect and offset geomorphic piercing lines (Figure 8), such as at channel thalwegs or interfluve crests offset by scarps at Sites 1 and 2. In order to capture the background piercing line geometry outside of the geomorphically modified fault zone, total station data were collected in the field every ∼0.5–1 m, to a distance of >20 m uphill and downhill of each fault scarp (Figures 4, 8, S9). We collected high-resolution profiles of offset geomorphic piercing lines where the three-dimensional oblique-slip vector could be calculated (n=24; Figures 4, 5, 6, S9; Lynch et al., 2025). We recognize that there can be some ambiguity and uncertainty in the position of the thalweg or interfluve (e.g., Zielke et al., 2010; Scharer et al., 2014) and that post-event processes such as erosion at a scarp crest and deposition against an uphill-facing scarp could alter the measurable earthquake-related offsets (e.g., Reitman et al., 2019). To address these uncertainties, we follow an approach similar to that used by Zielke et al. (2010) and Scharer et al. (2014). We asked several different users to select the "best" field-surveyed topographic points to use in our regressions, discussed below and in more detail in Supporting Information Text S3. In locations where channels and interfluves were absent, we collected linear topographic profiles with trends perpendicular to fault scarps to calculate the vertical (2D) component of displacement (n=6; Figures 5 and 6). We supplemented field profiles with profiles extracted from lidar topography (n=5; Figure 6). The majority of the 35 profiles cross multiple fault scarps.

Reliable calculation of a slip vector for any of the profile locations depends on constraining, as well as possible, the local orientation of the fault plane. No outcrop exposures of fault planes in Quaternary deposits were present in the field area, so we instead modeled the local strikes and dips of fault planes using a modified three-point problem approach. We assumed that the midpoints, or inflection points approximately halfway up a fault scarp, represent the most likely intersections of the fault plane with the surface. We surveyed scarp midpoints at multiple locations along each scarp and determined fault strike and dip through linear regression of a plane through the surveyed scarp midpoints using all survey data along a single, continuous fault strand segment (3–17 points per regression; see Supporting Information file for more details, and Figure 8). Fault strand regressions yielded predominantly NW-SE-striking, steeply NE-dipping faults at both Sites 1 and 2, with a few strands at Site 1 dipping steeply SW.

Once we had strike and dip of a fault plane (and uncertainties), the location where the fault plane intersects the ground surface, the XYZ coordinates of the topographic profile, and the number of points in the

upthrown and downthrown sides of the profile of the piercing line segments, we used a Monte Carlo-based R script (SCARP-3D; details in Supporting Information Text S3) to calculate 3D linear regressions through topographic profiles on the upthrown and downthrown sides of the fault scarp. We then used these regressions to solve for the intersection points of the linear regressions with the fault plane (Figure 8). The two intersection points were used to calculate the mean magnitudes and standard deviations of strike slip (SS), dip slip (DS), and oblique slip (OS) for each piercing line, as well as the trend and plunge of the slip. For the 6 sites without channel thalwegs or interfluve crests, we were able to calculate dip-slip—but not strike-slip—vectors.

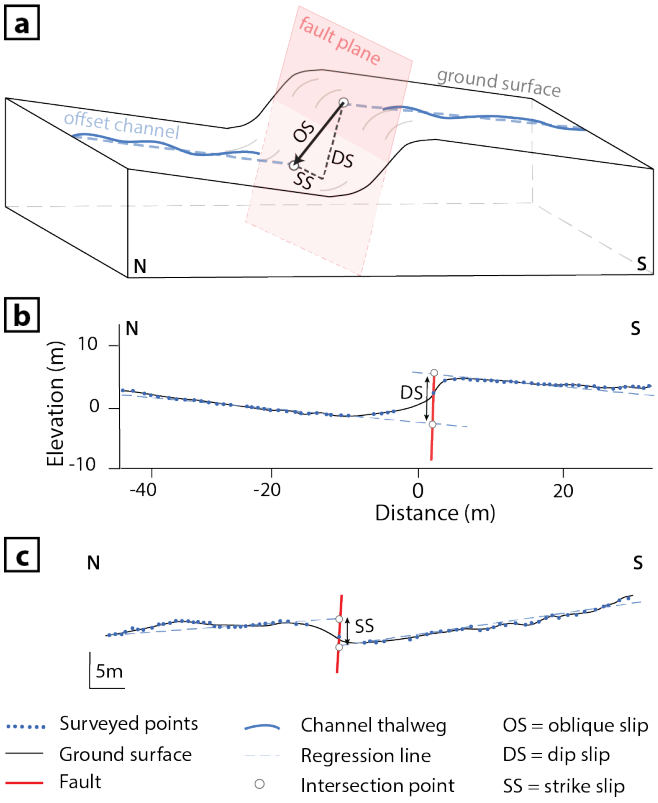

Figure 8 Schematic diagrams showing how surveyed geomorphic piercing lines were used to reconstruct 3D fault slip. **a:** Block diagram showing an oblique normal right-lateral offset channel thalweg. SCARP-3D calculates fault slip components (OS, DS, and SS) from the 3D positions of the intersections of the fault plane with the linear projections of the upthrown and downthrown channel segments. **b:** Example of a geomorphic piercing line profile in cross-section. **c:** Example of a geomorphic piercing line profile in plan view. In each profile, points were collected every ~0.5–1 m at least 10–20 m beyond the fault scarp.

7.2 Fault slip sense and displacement magnitudes

Our offset measurements suggest that the BRF fault system as a whole likely accommodates approximately equal magnitudes of strike slip and dip slip, but that some individual fault strands are dominated by dip slip, while others are dominated by strike slip (Table S2). Oblique-slip magnitudes across individual fault strands range from ~2 to 7 m at Site 1 and from ~2 to 5 m at Site 2, with strike slip to dip slip ratios ranging from ~0.3:1 to 1.5:1 (Figure 9; Table S2). Cumulative oblique slip magnitudes, calculated by summing displacements of a piercing line across multiple parallel strands at a site, range from 3.6–21.2 m at Site 1 and from 3.3–11.1 m at Site 2, with an average strike slip to dip slip ratio of 1.1:1 (Figures 9, 10). We note that cumulative oblique-slip magnitudes at Site 2 are likely underestimated, given that it was only possible to determine cumulative slip across a portion of the mapped strands due to limited access and preservation.

Our offset measurements show that slip magnitudes are greater along faults cutting older deposits than younger ones, indicating that older units have experienced at least one earthquake more. Figure 10a-b shows examples of this phenomenon at Sites 1.2 and 2.3. For example, along Strand D at Site 1.2 (location in Figure 5), vertical separation is 5.8 m along an offset interfluve developed in Qp1, the oldest offset deposit at the site, whereas only 4.7 m of vertical separation is present on the adjacent, younger channel incised into Qp1 (Figure 10a). Even less vertical separation (2.3 m) was observed where a younger Qft fluvial terrace crosses fault strand Ee (profile 3, Figure 5). Similarly, at Site 2.3, the till-mantled hillslope typically has larger vertical separation than channels incised into till (Figure 10b). For example, profile 28 at Site 2.3 in Qt shows 4.1 m of vertical separation across strand Q, whereas profile 33 along a younger channel incised into Qt shows only 2.9 m of vertical separation. These same relationships are mimicked in the set of cumulative right-lateral and oblique slip measurements at 23 interfluves and channels at Site 1 (Figure 9). Older interfluves developed in Qp1 are consistently associated with greater cumulative right-lateral and oblique slip than younger channels incised into Qp1 (Figure 10c). Average right-lateral and oblique slip magnitudes for interfluves are 8.8±3 m and 12.7±4.4 m, respectively, as compared to 4.8±3.4 m and 9.8±3.9 m in thalwegs.

7.3 Inversion for fault slip kinematics

We used slip vector data generated by SCARP-3D to invert for mean pressure- (P) and tension- (T) axes, as well as pseudo-focal mechanisms using Bingham statistics in FaultKin 7.6 (Marrett and Allmendinger, 1990; Allmendinger et al., 2012). In this inversion, slip is assumed to have occurred in the direction of maximum resolved shear stress on the fault plane (e.g., Angelier and Mechler, 1977; Riller et al., 2017). Outputs from these inversions may, under certain assumptions, be used to approximate local principal stress axis orientations at the time of deformation (e.g., Angelier and Mechler, 1977; Riller et al., 2017).

Kinematic inversions of all data from Sites 1 and 2, as well as inversions performed on subsets of data from individual sites, all yield right-lateral transtension (Figure 11). Slip vector data (n=50) yield an average slip vector of ~110°/45° along a NW striking, steeply NE-dipping fault (~300°/80°), with P- and T-axes at 170°/37° and 058°/26°

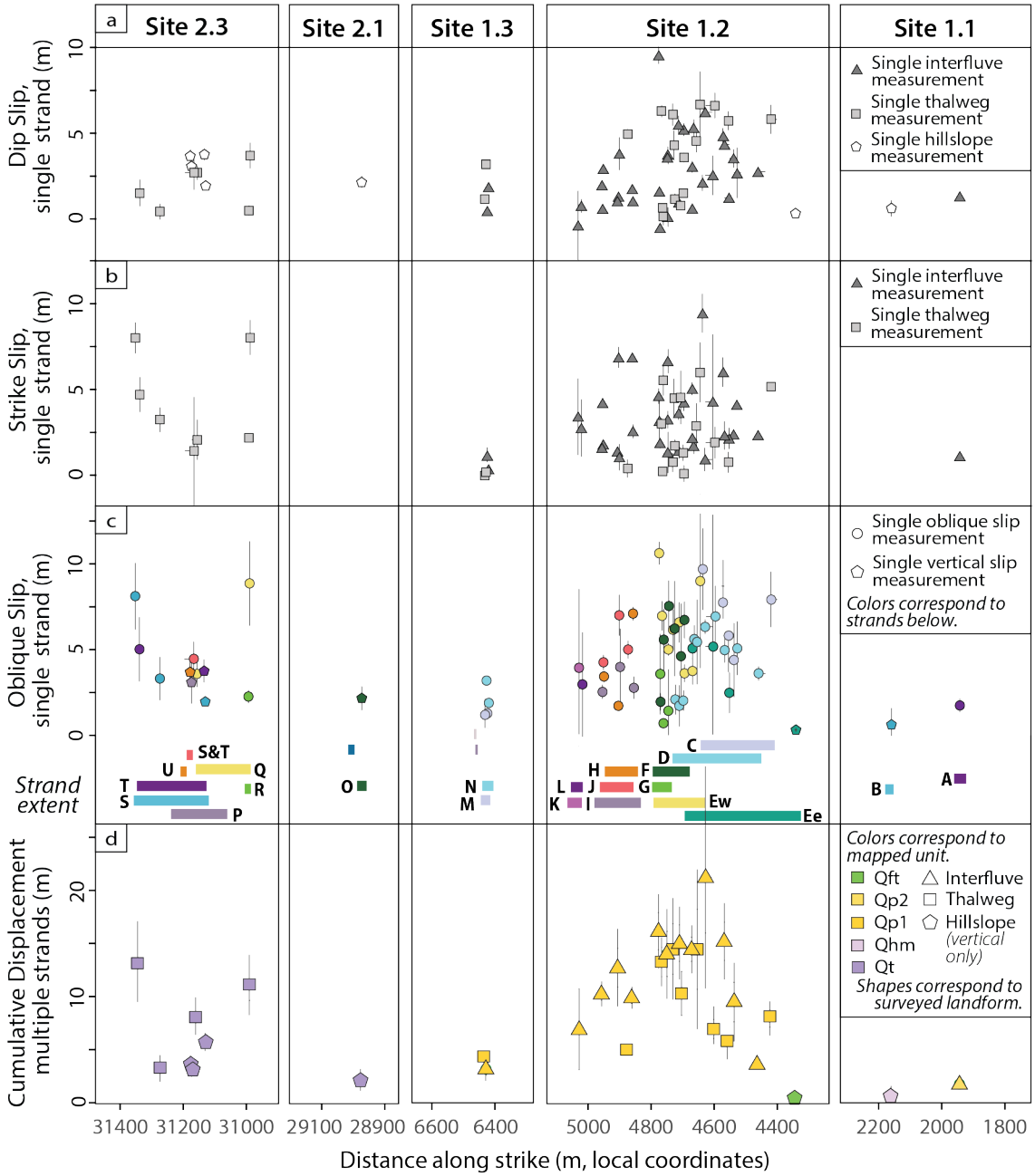

Figure 9 Displacement measured across the Beaufort Range fault at Sites 1 and 2. (2σ uncertainty) **a-c.** Magnitude of slip across single fault strands at given piercing points (dip slip in panel a, strike slip in panel b, and 3D oblique slip in panel c). Shapes in panels a and b correspond to the type of landform. Distance along strike is reported as the position where the piercing line crosses the fault strand. Colors in panel c correspond to individual fault strands, whose along-strike extents are also shown (see Figures 5 and 6 for locations). **d.** Summation of all of the slip vectors across all of the fault strands that a piercing line crosses. Distance along strike is the centroid distance of a profile relative to a local reference frame. Note that interfluve crests (triangles) show more displacement than channel thalwegs (squares). Colors in panel d correspond to the mapped unit (see Figure 3).

respectively (Figure 11e). Kinematic inversions of data subsets from individual sites yield only slight variations from this overall trend (Figure 11a-d).

8 Interpretation of the post-glacial history of the Beaufort Range fault

8.1 Evidence for an active fault

Our field data and observations provide evidence that the scarps we map along the southwestern flank of the Beaufort Range are tectonic in origin and are associated with slip along an active Beaufort Range fault. We identify 127 "valley-side up" scarps that offset multiple generations of Quaternary deposits and landforms (Figures 2b, 3). The scarps we map along the BRF define an ~500-m-wide zone of surface ruptures, spanning ~85 km of fault length, that we interpret to be the surficial expression of a throughgoing fault zone at depth. These scarps occur in en echelon and parallel arrays, clearly project into adjacent scarps across gaps and stepovers, and span several tens of kilometers of

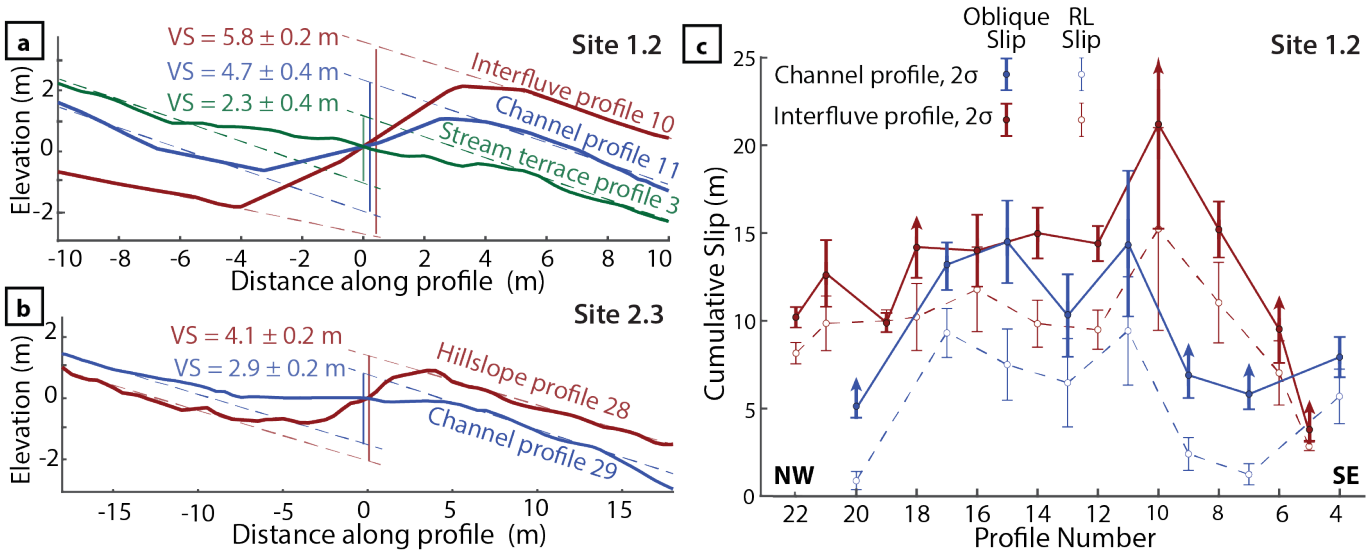

Figure 10 Topographic profiles showing larger magnitudes of offset in older Quaternary landforms than in younger ones. Profile locations shown in Figures 5, 6. **a.** Comparison of vertical separations (VS) from three piercing lines at Site 1.2. The red profile (profile 10, strand D) is from an interfluve developed in Qp1 (~11.5–9.5 cal ka BP). The blue profile (profile 11, strand D) is from a channel whose age correlates with Qp2 and is incised into Qp1 (~9.5 cal ka BP). The green profile (profile 3, strand Ee) is from a Holocene stream terrace (~3.5 cal ka BP). **b.** Comparison of vertical separations at Site 2.3. The red profile (profile 28, strand Q) is across a till-mantled hillslope (Qt, ~13.6–11.5 ka), and the blue profile (profile 29, strand Q) represents separation of a younger channel incised into till. **c.** Comparison of cumulative slip estimates from Site 1.2 profiles showing larger slip magnitudes for interfluve piercing lines than for channel thalwegs. Site 1.2 profiles extend ~800 m along strike (see Figure 5a). Solid, blue symbols and lines represent oblique slip across channel thalwegs. Open, blue symbols and dashed lines are cumulative, right-lateral (RL) slip estimates for faults across channels. Solid, red symbols and lines are for oblique slip across interfluves. Red, open symbols and dashed lines represent right-lateral slip across interfluves. Upward-pointing arrows indicate minimum slip estimates in locations where displacements across one or more strands could not be reconstructed.

strike length near the base of the Beaufort Range (Figures 2b, 4, 5, 6). Field observations show consistent vertical and lateral offsets across scarps at multiple independent sites, regardless of local topographic slopes, elevations above the valley floor, or bedrock versus Quaternary substrate. The three-dimensional, "V" shaped geometries of scarps as they cross interfluves and channels are consistent with formation by slip along a set of steeply dipping fault planes. Scarps in en echelon sets suggest formation in a right-lateral transtensional system, and kinematic inversions of slip recorded by offset piercing lines similarly yield pseudo-focal mechanisms consistent with right-lateral transtension along a steeply NE dipping fault plane (Figure 11).

The discontinuous nature of the mapped strands is likely due to the limited preservation potential of scarps that are developed in unconsolidated material, and occur in the steep terrain and wet climate characteristic of the Beaufort Range (e.g., Reitman et al., 2023), and the glacial history limiting preserved deposits to the past ~14 kyr. Similar discontinuous and distributed rupture patterns are documented elsewhere in the Cascadia forearc (e.g., along the North Olympic, Darrington Devils Mountain, Seattle, Leech River, and Boulder Creek faults, Personius et al., 2014; Sherrod et al., 2013; Nelson et al., 2003; Morell et al., 2017; Schermer et al., 2021), and in historical ruptures in subduction and non-subduction settings (e.g., Yuan et al., 2022; Li et al., 2012; Biasi and Wesnousky, 2016; Koral, 2000; Ainscoe et al., 2019; Bawden, 2001; Rodriguez Padilla et al., 2024). If all of the mapped scarps in this study are in fact associated with a continuous or even semi-continuous subsurface fault network, as we suggest, then the BRF would be the longest strike-length active fault identified in northern Cascadia to date.

8.2 Evidence for multiple, post-glacial, surface-rupturing earthquakes

Our results indicate that the BRF has hosted multiple surface-rupturing earthquakes since deglaciation of the Alberni Valley (~14–11 ka). This interpretation is supported by differential scarp heights and cumulative slip magnitudes calculated for offset landforms of different ages at Sites 1 and 2 (Figure 10). At Site 1, interfluve crests developed in the older paraglacial unit Qp1 have greater vertical separation (by ~1 m) and greater cumulative oblique slip (by ~1–3 m) than abandoned channel thalwegs incised into that same unit. The abandoned channels, in turn, have greater vertical separation (by ~2.4 m) than the displacement surveyed across a younger Qft fluvial terrace. The differential offset between interfluves, channels, and fluvial terraces suggests the occurrence of at least three earthquakes since the deposition of Qp1 at Site 1 (~13.6–9.5 ka; Figure S2). At Site 2, differential heights of ~2 m between scarps developed in till-mantled hillslopes versus younger channels incised into the hillslopes suggest at least two surface-rupturing earthquakes have occurred

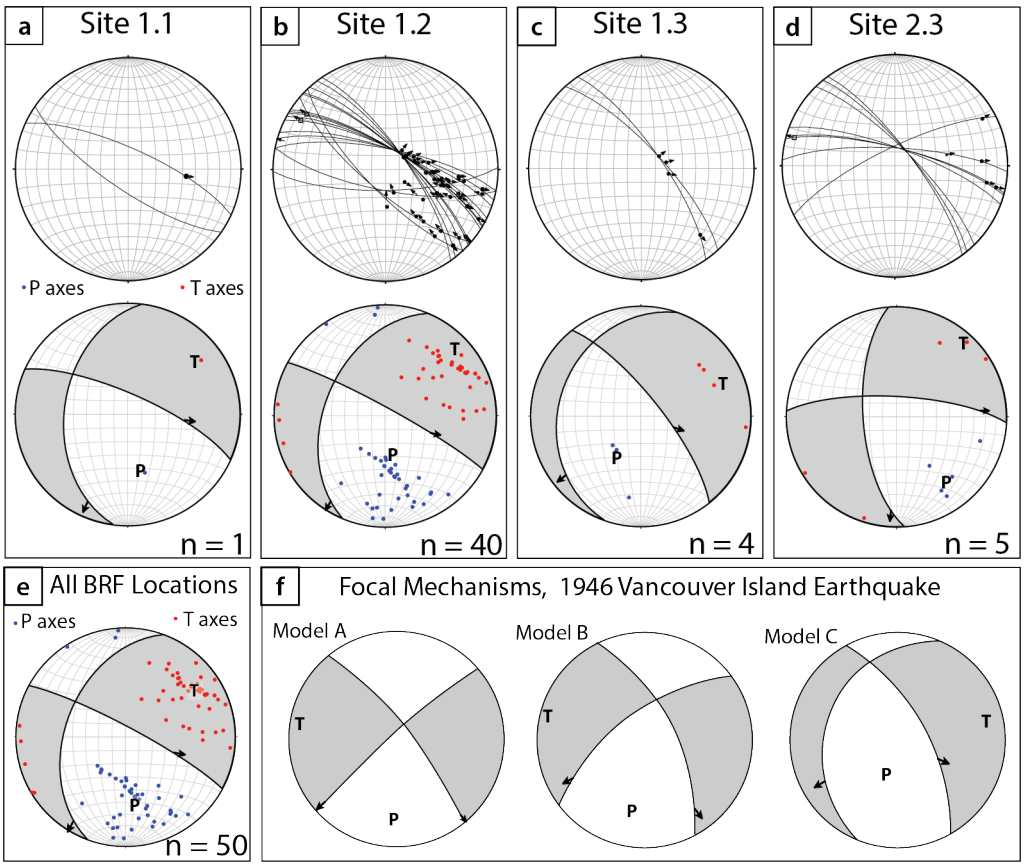

Figure 11 Right-lateral transtension along the Beaufort Range fault demonstrated by oblique slip of linear piercing points formed by paraglacial interfluves and channel thalwegs. Oblique-slip vectors and pseudo-focal mechanisms shown here are from kinematic inversions of detailed total station surveys of fault scarps and these offset geomorphic piercing lines. **a-d:** Kinematic data at four sub-sites along the BRF (see Figure 3 for locations). Upper panels: Lower hemisphere equal area projections showing fault planes, slip vectors, and hanging-wall motions. Lower panels: P- and T-axes and linked Bingham fault plane solutions for faults at Sites 1.1, 1.2, 1.3, and 2.3. These slip vectors and kinematic inversions are consistent with right-lateral oblique motion on northeast-dipping planes. **e:** Composite kinematic inversion for all surveyed sites along the BRF. Lower hemisphere equal area projection showing P- and T-axes and linked Bingham fault plane solutions. **f:** Focal mechanism solutions for the 1946 M 7.3 Vancouver Island earthquake (see Figure 2a for epicentral location; Rogers and Hasegawa, 1978). Model A is Rogers and Hasegawa's preferred model. Note the similarity in orientations of nodal planes and P- and T-axes for BRF fault kinematics.

at Site 2 following the deposition of Qt (~13.6–11 ka).

While the difference in cumulative vertical separation between landforms of different ages is relatively small, on the order of 1–2 m, this difference is reproducible across 8 out of the 12 measured profiles spanning ~800 m in distance at Site 1. These 1–2 m differences in offsets are an order of magnitude larger than the absolute measurement uncertainty of the total station primary topographic data (<1 cm) or the inherent roughness of the forest floor (typically 10s of centimeters but rarely at most 50 cm). We focus on the smaller abandoned channels in this study because the major drainages on the Beaufort Range are extremely active seasonally, and have enough discharge to occasionally move large boulders. Therefore, the larger streams have more than enough power to erode through scarps and straighten out their profiles compared to observed offsets on the BRF.

If the average difference we observe in cumulative oblique slip between interfluves and channels (1–2.4 m) is the result of at least one event, we can estimate the minimum number of events necessary to produce the total observed slip in the oldest offset deposits. If one earthquake produces 1–2.4 m of slip, the cumulative oblique-slip offsets of 10–15 m may be the product of three or more earthquakes since ~11–14 ka. This inference is corroborated by displacement-length scaling relationships. For faults with lengths of 35–100 km, as we map for the BRF, a single earthquake is predicted to result in an average surface slip of 0.4–3 m (Wells and Coppersmith, 1994; Wesnousky, 2008), and thus our total offsets of 10–15 m are consistent with three or more events.

If our three-event interpretation is correct, we can broadly constrain the timing of earthquakes by combining our estimates of deposit ages at Site 1 (Table 1; Figure 3c) with offset magnitudes (Table S2; Figures 9, 10). The first earthquake occurred after the deposition of Qp1 (<11–14 ka), but before the abandonment of channels incised into Qp1, because the cumulative oblique offset is larger in interfluves developed in Qp1 than in channels subsequently incised into Qp1 (Figure

9; Figure S2). The timing of channel abandonment is not directly dated, but our correlation of channel incision to the deposition of Qp2 suggests channel abandonment occurred after the deposition of Qp2 (radiocarbon dated to ∼11 to 6 ka) and before the deposition of Qaf (radiocarbon dated to ∼6–3 ka). Therefore, the first earthquake(s) likely occurred after ∼11–14 ka, but before ∼6–3 ka. The second earthquake occurred after channel abandonment and before the development of the fluvial terrace at Site 1, based on the difference in offset between channels and inset Qft terraces (Figure 9; Figure S2). Our estimate of the age of channel abandonment and the radiocarbon age obtained from terrace deposits indicates the second earthquake likely occurred after 11–6 ka but before <4 ka. The third earthquake occurred after the deposition of the offset Qft terrace at Site 1. The radiocarbon age acquired from Qft suggests the third earthquake occurred after ∼4 ka.

We note that the above estimates rely on the assumption that landscape adjustment to fault offset occurs at similar rates on interfluves and channels. It is possible that offset magnitudes in channels underestimate total slip due to differential scarp degradation and sediment ponding, and may not solely be the product of slip during different numbers of events. We note, however, that even if we discount the differential offset of interfluves and channels, the total scarp height and oblique slip in interfluves, displacement-length scaling estimates, and differences in offset between Qp1 and Qt depositions still suggest multiple earthquakes on the BRF since the Late Pleistocene.

8.3 Estimates of earthquake magnitudes and post-glacial slip rates

Estimates of earthquake magnitudes and fault slip rates are primary data used for seismic hazard analyses (e.g., Morell et al., 2020; Hatem et al., 2022) and can yield important information about how strain is partitioned across multiple faults in a system. Despite uncertainties on slip magnitudes for individual earthquakes and on earthquake ages, we can place rough bounds on the magnitudes of past earthquakes and the post-glacial (<10–14 ka) slip rate for the BRF.

We can use displacement-length scaling relationships to constrain paleo earthquake magnitudes using either the estimated slip per earthquake or the total length of the active fault (Wells and Coppersmith, 1994; Wesnousky, 2008). The ∼1–3 m of slip per earthquake we infer suggests that the BRF could have hosted M_W 6.9 to 7.2 earthquakes. This range is very similar to that corresponding to our mapped fault length of 35–85 km, which suggests M_W 6.8 to 7.4 earthquakes. Such earthquake magnitudes are similar in scale to the M 7.3 magnitude calculated for the 1946 Vancouver Island earthquake (Rogers and Hasegawa, 1978), which caused significant damage, including to telephone wires, underwater telegraph cables, and the hospital in Port Alberni, BC (Hodgson, 1946). An earthquake of a similar magnitude today would pose a significant hazard not only to Port Alberni, but also to the nearby communities of Nanaimo, Parksville, Qualicum Beach, and Courtenay, and dams on Comox Lake and Elsie Lake (Figure 2a).

Furthermore, we can use our constraints of unit ages and event timing to estimate slip rates for the BRF. Ideally, slip rates are calculated from two or more precise earthquake ages and the slip magnitude associated with each (e.g., Working Group on California Earthquake Probabilities, 1990; Hatem et al., 2025). In the absence of precise earthquake ages that can be used to calculate a closed-interval slip rate (e.g., Styron, 2019; DuRoss et al., 2020), an open-interval slip rate can be estimated by dividing the cumulative displacement of a dated landform by its age. Open-interval estimates yield minimum slip rates because the time elapsed since the most recent slip event is unknown, as is the time elapsed between surface formation and displacement (e.g., Hatem et al., 2025). We note that both closed- and open-interval slip rates can be underestimated if there is considerable off-fault deformation (e.g., Harrichhausen et al., 2023a; Styron, 2019).

We have applied both approaches for our Site 1 data, where we have evidence for at least three earthquakes and associated slip vectors. Both open-ended and closed-interval approaches yield slip rates for the BRF that range from ∼0.5 to ∼2 mm/yr. The open-ended approach yields an oblique slip rate of ∼0.7–1.3 mm/yr, based on the ∼10 to 15 m of cumulative oblique slip across all mapped fault strands and an estimated deglaciation age of ∼13.6–11.5 ka. Just one closed-interval calculation can be made, using the ∼8–9 m of cumulative displacement of channels at Site 1 and the difference in age between the Qft terrace and the interfluves, which could range from ∼3.5 to 13.6 kyr. This yields a slip rate estimate of 0.6–2.6 mm/yr.

Our data demonstrate that, even at the lower bound of uncertainty, the Beaufort Range fault is one of the fastest slipping active faults in the northern Cascadia forearc. Our slip rate estimates of ∼0.5 to ∼2 mm/yr indicate that the BRF has a higher slip rate than the nearby Leech River fault (0.2–0.3 mm/yr; Morell et al., 2017, 2018) and the Darrington-Devils Mountain fault zone (0.14 ± 0.1 mm/yr; Personius et al., 2014), and a similar slip rate to the North Olympic fault zone (1.3–2.3 mm/yr, 3–5 post-glacial earthquakes; Schermer et al., 2021). This observation indicates that the BRF is a major crustal structure accommodating permanent deformation in the northern Cascadia forearc.

8.4 Slip on the BRF compared with the kinematics of the 1946 earthquake

Late Pleistocene to Holocene faulting along a NW-SE striking, steeply NE dipping active BRF is kinematically and spatially compatible with the slip inferred from seismic wave inversions for the 1946 Vancouver Island earthquake (Figure 11). The attitudes of nodal planes produced in our kinematic slip inversions (∼300°/80°NE and ∼200°/40°NW) have similar geometries to the NW-SE and NE-SW striking nodal planes reported for the 1946 earthquake (320°/80°NE and 230°/85°NW; Rogers and Hasegawa, 1978; Figure 11f, Table S3). Our predicted slip vectors associated with the NW-SE striking nodal planes have trends of 096-135° and plunges of 10-

48°, similar to the ranges published for the 1946 earthquake (trends of 114 to 183° and plunges from 05 to 54°). Additionally, the stress axes determined for the 1946 focal mechanism solutions have moderately plunging, southerly trending P-axes and sub-horizontal T-axes with trends similar to those determined for the active BRF (Figure 11).

Our fault slip vectors and transtensional pseudo-focal mechanisms for the BRF are also similar to fault plane inversions based on geodetic motions associated with the 1946 earthquake (Slawson and Savage, 1979). Repeat surveys of topographic benchmarks across the Beaufort Range at the latitude of the earthquake epicenter (∼49.45° N) suggest ∼1–2.5 m of right-lateral oblique slip on a steeply (70°) NE-dipping fault plane that extended for 60 km along strike (Slawson and Savage, 1979). Our mapped Sites 1 and 2 along the BRF lie within the modeled earthquake rupture area, and the fault plane dip is similar to the 60–88° NE dip we determined for the BRF. In addition, slip inversions for the 1946 earthquake fault planes indicate the crustal slip is best reproduced by ∼1 m of right-lateral and ∼2 m dip slip, along 60 km of fault length parallel to the BRF at 0–5 km depth (Slawson and Savage, 1979). Therefore, both the relative ratio of strike slip to dip slip (∼0.5:1) and the estimated slip per earthquake (∼1–2 m) modeled for the 1946 earthquake are similar to our slip ratios of 0.3–1.5:1 and estimates of ∼1–3 m of oblique slip per BRF earthquake.

These correlations suggest that, if the 1946 event ruptured along a northwest-southeast striking, steeply northeast-dipping plane, as suggested by Rogers and Hasegawa (1978) and Slawson and Savage (1979), the BRF is a likely candidate for hosting the 1946 event. It is worth noting that no other candidate fault has been identified. Our estimated age of the most recent event of <3–4 ka allows for this possibility. However, the field data reported here cannot constrain the timing of the most recent event along the active BRF beyond that it occurred after ∼3–4 ka, and therefore cannot conclusively test whether the 1946 event ruptured along the BRF within our field area.

8.5 Relationship of the active BRF to inherited structures

The proximity of the strands of mapped BRF scarps to the surface trace of the Eocene bedrock fault suggests the possibility that the recent deformation we observed reflects reactivation of that Eocene thrust fault plane. However, several lines of evidence suggest that the surface trace of the mapped bedrock thrust fault has not experienced slip since the Late Pleistocene. First, none of the recent scarps we identified exactly coincide with the mapped Eocene fault. Some scarps are up to 500 m away from the Eocene bedrock thrust fault and occur in both the hanging wall and footwall of the fault (Figure 3). Second, active fault strands have different geometries and kinematics than the Eocene bedrock thrust fault. Fault plane strikes on active scarps differ by as much as 15° from those on the Eocene fault (Figures 3 and S6). Slip senses on active strands require NE-side-down motion on steeply dipping faults (60-80°), whereas bedrock fault exposures, seismic reflection profiles, exhumation histories, and balanced cross sections indicate NE-side-up slip on the bedrock thrust fault on a moderately (45-60°) dipping fault plane (e.g., Yorath et al., 1985a; Clowes et al., 1987; England and Calon, 1991). Third, we observed at several sites that Quaternary deposits were not offset across the Eocene fault (Figure S7). These observations suggest that the BRF and Eocene thrust fault do not share a principal slip surface, at least at the ground surface.

We postulate several scenarios that may explain the relationship between the active BRF and the Eocene bedrock thrust fault. We consider the possibility that the active BRF could be a bending moment fault accommodating extension in the shallow layers of active, thrust fault-related antiforms due to thrust slip on the Eocene fault (e.g., Philip and Meghraoui, 1983). Our field observations, however, preclude this scenario because we found no evidence of antiformal folding of Karmutsen, Nanaimo, or Quaternary formations, nor did we find evidence of thrust-sense offset of Quaternary deposits anywhere along the fault. Instead, we consider one of the two following scenarios more likely. The active BRF could reactivate the Eocene fault if steeply dipping (60-80°) BRF faults in the near surface merge with the more gently dipping (45-60°) Eocene fault at depth. This scenario requires that the bedrock thrust fault has changed slip sense since the Eocene, and now accommodates right-lateral transtension. Alternatively, the subsurface projections of the steep active BRF and more gentle Eocene bedrock faults could diverge at depth. Similar instances of new faults cutting across ancient, now inactive faults have been reported for the northern Cascadia forearc along the Leech River and North Olympic faults (Morell et al., 2017; Li et al., 2018a; Nelson et al., 2017; Schermer et al., 2021).

Finally, we also consider the apparent discrepancy between the NE-side-up topography of the Beaufort Range and the NE-side-down slip sense we determined for the active BRF. It is likely that much of the relief on the western side of the Beaufort Range is the product of differential erosion of the softer Cretaceous Nanaimo Gp. sediments that underlie the Alberni Valley, relative to the more resistant Karmutsen Fm. basalts that underlie the range crest (Muller and Carson, 1969). Such differential erosion would be consistent with typical glacial valley morphology, and would suggest that the inherited structure of the bedrock in the hanging wall of the Eocene bedrock thrust is a major control on the morphology of the Beaufort Range. These observations may also indicate that slip on the active BRF is a relatively young phenomenon, and that the cumulative magnitude of NE-side-down motion on the active BRF is too small to generate large topographic relief.

8.6 Implications for forearc stress state and strain accommodation

The results of our work demonstrate that this portion of the Cascadia forearc has experienced permanent, right-lateral transtensional deformation for at

least ∼11–14 kyr. This interpretation is supported by the similarity between geologically determined fault kinematics, integrated over multiple Late Pleistocene to Holocene earthquakes, and the seismically and geodetically determined kinematics for the 1946 Vancouver Island earthquake. In addition, P- and T-axes from kinematic slip inversions for the active BRF and those inverted for the 1946 Vancouver Island earthquake (Figure 11) are consistent with regional stress patterns derived from historical seismicity (Figure 2a; Balfour et al., 2011). These data suggest that a transtensional stress state has persisted in the northern Cascadia forearc over both millennial and decadal timescales in the Quaternary. Given that recurrence rates for upper-plate fault seismic cycles are likely on the order of 1000s of years (e.g., Morell et al., 2018; Schermer et al., 2021), and megathrust cycles have recurrence intervals of ∼390–540 years (e.g., Walton et al., 2021), the deformation we observed must represent a long-term, regional stress pattern, rather than the type of short-lived change that results from timing within the megathrust seismic cycle (e.g., Wang et al., 1995; Loveless et al., 2010; Regalla et al., 2017).

The persistence of right-lateral transtensional earthquakes throughout the Late Pleistocene to present indicates that tectonic forces are the principal drivers of deformation along the BRF, rather than changes in crustal loads and viscoelastic relaxation of the crust and mantle, as documented in other glaciated regions (e.g., Anderson et al., 1989; Lagerbäck, 1990; Muir-Wood, 2000). Such "glacially-induced" earthquakes typically occur during or within 3–6 kyr of glacial retreat, when changes in ice loads and crustal stresses from the viscoelastic rebound are most rapid (Steffen et al., 2014), but deformation along the BRF has continued for 7 to >10 kyr after deglaciation of the Alberni Valley. Additionally, we note that glacial unloading typically reduces vertical stress, and given that our slip data indicate the BRF accommodates transtension, such unloading would reduce the deviatoric stress, making failure less likely. Thus, any stress changes due to glacial unloading are likely secondary to the primary tectonic forces promoting transtensional deformation in the north Cascadia forearc.

Comparison of displacements on the Eocene bedrock thrust fault in the Beaufort Range and the active BRF indicates that stress field conditions in this portion of the northern Cascadia forearc have changed since the Eocene from contraction to right-lateral transtension. Eocene contraction was the product of the accretion of the Crescent and Pacific Rim terranes to the North America plate, which led to the development of the Cowichan fold and thrust belt, including the Eocene bedrock thrust in the Beaufort Range (England and Calon, 1991; Harrichhausen et al., 2022). This deformation ended by ∼40 Ma, when subduction of the Juan de Fuca plate was established (England et al., 1997; Madsen et al., 2006).

The right-lateral transtension documented on the BRF on Vancouver Island differs from the right-lateral transpression documented on forearc faults farther south in the northern forearc (the Darrington-Devils Mountain, Southern Whidbey Island, Leech River, and XEOLXELEK-Elk Lake faults, Figures 1, 2a; Sherrod et al., 2008; Personius et al., 2014; Schermer et al., 2021; Morell et al., 2018; Harrichhausen et al., 2021, 2023b). Kinematic data alone, as we present here, are insufficient to determine the causes of this difference. However, we offer two potential factors that could explain the spatial variation in strain accommodation. First, paleomagnetic data and geodetic rotations show active bending of the Olympic Orocline, such that the northern Cascadia forearc of central and northern Vancouver Island has been rotating counterclockwise since ∼18 Ma (Wells et al., 1998; Johnston and Acton, 2003; Finley et al., 2019; Harrichhausen et al., 2021). Counterclockwise rotation of the forearc on Vancouver Island away from the stable continental interior could explain the transtension that drives deformation on the BRF on central Vancouver Island. Second, transtension may be related to changes in convergence rate or obliquity related to the northward migration of the northern terminus of the Juan de Fuca plate and the ∼4 Ma formation of the Explorer microplate (Madsen et al., 2006; Wells et al., 1998; Wang, 2000; McCaffrey et al., 2013; Li et al., 2018b; Audet et al., 2008). Kinematic data from the BRF alone, however, are insufficient to distinguish the relative contributions of these different processes. Regardless of cause, these kinematic data are consistent with persistent transtensional deformation over millennial and decadal timescales, along active, hazardous faults in the northern Cascadia forearc.

9 Conclusions

We provide the first geologic field evidence for a major active fault on central Vancouver Island with constraints on the kinematics, deformation rates, and state of stress in this portion of the northern Cascadia forearc. Field mapping and topographic profiles along the Beaufort Range fault (BRF) document >35 km of NW-striking, primarily NE-dipping fault strands along the southwestern flank of the Beaufort Range that offset Late Pleistocene to Holocene post-glacial deposits. We observe an increase in scarp height and total offset with increasing unit age that provides evidence for at least three surface-rupturing earthquakes on the BRF since ∼13.6–11 ka, the most recent of which occurred in the past ∼3–4 kyr. Slip magnitudes reconstructed from offset piercing lines, total fault length, and the ages of offset deposits suggest that the BRF is capable of hosting earthquakes of M_W 6.5–7.5, and has a Late Pleistocene to Holocene slip rate of 0.5 to 2 mm/yr. Notably, kinematic slip inversions for the BRF yield transtensional pseudo-focal mechanisms, fault geometries, slip vectors, and P- and T-axes that are all similar to those determined for the 1946 Vancouver Island earthquake, suggesting that the BRF may have hosted that damaging earthquake. The consistency of right-lateral transtensional slip kinematics between the 1946 earthquake and Late Pleistocene to Holocene slip on the BRF suggests that this portion of the northern Cascadia forearc has accommodated regional transtension over decadal to millennial time scales, spanning multiple earthquake

cycles.

Acknowledgements

This work was conducted on the traditional territory of the Hupačasath, K'ómoks, and ćišaaʔath people, and we acknowledge their historical relationships with the land that continue to this day. Funding for this project was supported by NSF EAR Tectonics 1756834/ 2004684 to Regalla and 1756943 to Morell, by the Boston University Department of Earth and Environmental Sciences, and the Northern Arizona University Duebendorfer-Barnes Structure Endowment. We would like to thank Todd Thompson, TimberWest, and Island Timberlands for land access, and Mosaic/Island Timberlands/TimberWest for providing lidar ground return data. We would like to thank Scott Bennett for illuminating discussions in the office and field and Edwin Nissen and the University of Victoria School of Earth and Ocean Sciences for discussion of local tectonics and help with field logistics. We would also like to acknowledge the late Vic Levson for help with understanding glacial systems of Vancouver Island, and Johanna Fischi and Tatum McLeod for assistance in the field. This paper benefited from comments from Nadine Reitman, Ian Pierce, Stephen Angster, and Alan Nelson, as well as from Editor Jason Padgett, and from the editing services of Dr. Laura Wasylenki.

Data and code availability

New data produced in this study:

Data collected and analyzed in this manuscript are available in a Dryad Data Repository (Lynch et al., 2025) at: https://doi.org/10.5061/dryad.nvx0k6dvc. The repository contains the following data:

1. Text files containing raw field data (x,y,elevation) of surveyed offset landforms
2. Text files containing raw field data (x,y,elevation) of fault midpoint locations
3. R script for calculating 3D fault plane geometry (SCARP-3D)
4. R script for calculating 3D offsets of linear piercing lines across a dipping fault

Previously published data and programs used in this study:

1. Lidar is available through LidarBC at https://lidar.gov.bc.ca/.
2. The USGS Quaternary faults and folds database used for Figure 1 is available at https://www.usgs.gov/programs/earthquake-hazards/faults.
3. The BC Geological Survey (BCGS) bedrock geology map used for Figures 2a and 3 is available at https://www2.gov.bc.ca/gov/content/industry/mineral-exploration-mining/british-columbia-geological-survey/geology/bcdigitalgeology.
4. The OxCal program v. 4.4 by C. Bronk Ramsey used for radiocarbon calibration is available at https://c14.arch.ox.ac.uk/oxcal/OxCal.html.
5. The R. Allmendinger FaultKin 7.6 program used for plotting and analyzing fault plane and slip vector data in Figure 11 is available at https://www.rickallmendinger.net/faultkin.
6. The OSX Stereonet 9.9.4 program used for plotting bedrock fault planes and slickenlines in Figure S6 is available at https://www.rickallmendinger.net/stereonet.

Competing interests

The authors state that they have no competing interests.

References

Ainscoe, E. A., Abdrakhmatov, K. E., Baikulov, S., Carr, A. S., Elliott, A. J., Grützner, C., and Walker, R. T. Variability in surface rupture between successive earthquakes on the Suusamyr Fault, Kyrgyz Tien Shan: implications for palaeoseismology. *Geophysical Journal International*, 216(1):703–725, 2019. doi: 10.1093/gji/ggy457.

Alley, N. F. and Chatwin, S. C. Late Pleistocene history and geomorphology, southwestern Vancouver Island, British Columbia. *Canadian Journal of Earth Sciences*, 16(9):1645–1657, 1979. doi: 10.1139/e79-154.

Allmendinger, R. W., Cardozo, N., and Fisher, D. M. *Structural geology algorithms: Vectors and tensors in structural geology*. Cambridge University Press, 2012.

American Geosciences Institute. Global GIS: Volcanoes of the world, 2003. https://earthworks.stanford.edu/catalog/harvard-glb-volc.

Anderson, W. A., Borns, H. W., Kelley, J. T., and Thompson, W. B. Neotectonic activity in coastal Maine. *Maine Geological Survey*, pages 195–212, 1989.

Angelier, J. and Mechler, P. Sur une methode graphique de recherche des contraintes principales egalement utilisables en tectonique et en seismologie: la methode des diedres droits. *Bulletin de la Société Géologique de France*, S7-XIX(6): 1309–1318, 1977. doi: 10.2113/gssgfbull.S7-XIX.6.1309.

Audet, P., Bostock, M. G., Mercier, J. P., and Cassidy, J. F. Morphology of the Explorer-Juan de Fuca slab edge in northern Cascadia: Imaging plate capture at a ridge-trench-transform triple junction. *Geology*, 36(11):895–898, 2008. doi: 10.1130/G25356A.1.

Balfour, N. J., Cassidy, J. F., Dosso, S. E., and Mazzotti, S. Mapping crustal stress and strain in southwest British Columbia. *Journal of Geophysical Research: Solid Earth*, 116(3):1–11, 2011. doi: 10.1029/2010JB008003.

Ballantyne, C. K. A general model of paraglacial landscape response. *The Holocene*, 12:371–376, 2002. doi: 10.1191/0959683602hl553fa.

Ballantyne, C. K. and Benn, D. I. Paraglacial slope adjustment during recent deglaciation and its implications for slope evolution in formerly glaciated environments. In Brooks, S. and Anderson, M., editors, *Advances in Hillslope Processes*, volume 2, pages 1173–1195. Wiley, 1996.

Bawden, G. W. Source parameters for the 1952 Kern County earthquake, California: A joint inversion of leveling and triangulation

observations. *Journal of Geophysical Research: Solid Earth*, 106 (B1):771–785, 2001. doi: 10.1029/2000JB900315.

Benavente, C., Palomino, A., Wimpenny, S., Garcia, B., Rosell, L., Aguirre, E., Macharé, J., Padilla, A. M. R., and Hall, S. R. Paleoseismic evidence of the 1715 CE earthquake on the Purgatorio Fault in Southern Peru: Implications for seismic hazard in subduction zones. *Tectonophysics*, 834:229355, 2022. doi: 10.1016/j.tecto.2022.229355.

Biasi, G. P. and Wesnousky, S. G. Steps and gaps in ground ruptures: Empirical bounds on rupture propagation. *Bulletin of the Seismological Society of America*, 106(3):1110–1124, 2016. doi: 10.1785/0120150175.

Blaise, B., Clague, J. J., and Mathewes, R. W. Time of maximum Late Wisconsin glaciation, west coast of Canada. *Quaternary Research*, 34(3):282–295, 1990. doi: 10.1016/0033-5894(90)90041-l.

Brodzikowski, K. and van Loon, A. J. A systematic classification of glacial and periglacial environments, facies and deposits. *Earth Science Reviews*, 24(5):297–381, 1987. doi: 10.1016/0012-8252(87)90061-4.

Bronk Ramsey, C. Radiocarbon calibration and analysis of stratigraphy: The OxCal program. *Radiocarbon*, 37(2):425–430, 1995. doi: 10.1017/s0033822200030903.

Bronk Ramsey, C. OxCal Program, Version 4.4, 2021.

Clague, J. J. Quaternary stratigraphy and history of south-coastal British Columbia. *Geological Survey of Canada Bulletin*, 481: 181–192, 1994.

Clague, J. J. Paleoseismology and seismic hazards, southwestern British Columbia. *Geological Survey of Canada Bulletin*, 494, 1996.

Clague, J. J. and James, T. S. History and isostatic effects of the last ice sheet in southern British Columbia. *Quaternary Science Reviews*, 21:71–87, 2002. doi: 10.1016/S0277-3791(01)00070-1.

Clague, J. J. and Ward, B. Pleistocene Glaciation of British Columbia. In Ehlers, J., Gibbard, P. L., and Hughes, P. D., editors, *Developments in Quaternary Sciences*, volume 15 of *Quaternary Glaciations - Extent and Chronology*, pages 563–573. Elsevier, 2011. doi: 10.1016/B978-0-444-53447-7.00044-1.

Clague, J. J., Armstrong, J. E., and Mathews, W. H. Advance of the late Wisconsin Cordilleran Ice Sheet in southern British Columbia since 22,000 Yr B.P. *Quaternary Research*, 13(3): 322–326, 1980. doi: 10.1016/0033-5894(80)90060-5.

Clowes, R. M., Brandon, M. T., Green, A. G., Yorath, C. J., Brown, A. S., Kanasewich, E. R., and Spencer, C. LITHOPROBE - southern Vancouver Island: Cenozoic subduction complex imaged by deep seismic reflections. *Canadian Journal of Earth Sciences*, 24:31–51, 1987. doi: 10.1139/e87-004.

Cui, Y., Miller, D., Schiarizza, P., and Diakow, L. British Columbia digital geology. Technical Report 2017-8, British Columbia Ministry of Energy, Mines and Petroleum Resources, 2017.

Delano, J. E., Amos, C. B., Loveless, J. P., Rittenour, T. M., Sherrod, B. L., and Lynch, E. M. Influence of the megathrust earthquake cycle on upper-plate deformation in the Cascadia forearc of Washington State, USA. *Geology*, 45(11):1051–1054, 2017. doi: 10.1130/G39070.1.

DeMets, C., Gordon, R. G., and Argus, D. F. Geologically current plate motions. *Geophysical Journal International*, 181(1):1–80, 2010. doi: 10.1111/j.1365-246X.2009.04491.x.

Duckworth, W. C., Amos, C. B., Schermer, E. R., Loveless, J. P., and Rittenour, T. M. Slip and strain accumulation along the Sadie Creek fault, Olympic Peninsula, Washington. *Journal of Geophysical Research: Solid Earth*, 126(3), 2021. doi: 10.1029/2020JB020276.

DuRoss, C. B., Gold, R. D., Briggs, R. W., Delano, J. E., Ostenaa, D. A., Zellman, M. S., Cholewinski, N., Wittke, S. J., and Mahan, S. A. Holocene earthquake history and slip rate of the southern Teton fault, Wyoming, USA. *GSA Bulletin*, 132(7-8):1566–1586, 2020. doi: 10.1130/B35363.1.

Easterbrook, D. J. Advance and retreat of Cordilleran ice sheets in Washington, U.S.A. *Géographie Physique et Quaternaire*, 46 (October):51–68, 1992. doi: 10.7202/032888ar.

England, T. D. J. *Late Cretaceous to Paleogene evolution of the Georgia Basin, southwestern British Columbia*. Ph.D. Thesis, University of British Columbia, 1990.

England, T. D. J. and Calon, T. J. The Cowichan fold and thrust system, Vancouver Island, southwestern British Columbia. *Geological Society of America Bulletin*, 103(3):336–362, 1991. doi: 10.1130/0016-7606(1991)103<0336:TCFATS>2.3.CO;2.

England, T. D. J., Currie, L. D., Massey, N. W., Roden-Tice, M. K., and Miller, D. S. Apatite fission-track dating of the Cowichan fold and thrust system, southern Vancouver Island, British Columbia. *Canadian Journal of Earth Sciences*, 34(5):635–645, 1997. doi: 10.1139/e17-050.

Eyles, N., Boyce, J. I., and Barendregt, R. W. Hummocky moraine: Sedimentary record of stagnant Laurentide Ice Sheet lobes resting on soft beds. *Sedimentary Geology*, 123(3-4):163–174, 1999. doi: 10.1016/S0037-0738(98)00129-8.

Finley, T., Morell, K. D., Leonard, L., Regalla, C., Johnston, S. T., and Zhang, W. Ongoing oroclinal bending on the Cascadia forearc margin and its relation to concave-outboard plate margin geometry. *Geology*, 47(2):155–158, 2019. doi: 10.1130/G45473.1.

Fyles, J. G. Surficial geology of Horne Lake and Parksville map-areas, Vancouver Island, British Columbia. *Geological Survey of Canada Memoir*, 318:142, 1963.

Gao, D., Wang, K., Davis, E. E., Jiang, Y., Insua, T. L., and He, J. Thermal state of the Explorer segment of the Cascadia subduction zone: Implications for seismic and tsunami hazards. *Geochemistry, Geophysics, Geosystems*, 18(4):1569–1579, 2017. doi: 10.1002/2017GC006838.

Google Earth Pro. Alberni Region, BC Canada. 49°22'31.59"N, 124°53'50.52"W, Landsat, Copernicus., Dec. 2016. http://www.google.com/earth/index.html.

Graham, A. Geometry, kinematics, and Quaternary activity of the Leech River fault zone, southern Vancouver Island, British Columbia, Canada. Master's thesis, University of Victoria, 2017.

Halsted, E. C. The Cowichan ice tongue, Vancouver Island. *Canadian Journal of Earth Sciences*, 5:1409–1415, 1968.

Hardebeck, J. L. and Okada, T. Temporal Stress Changes Caused by Earthquakes: A Review. *Journal of Geophysical Research: Solid Earth*, 123(2):1350–1365, 2018. doi: 10.1002/2017JB014617.

Harrichhausen, N., Morell, K. D., Regalla, C., Bennett, S. E., Leonard, L. J., Lynch, E. M., and Nissen, E. Paleoseismic trenching reveals Late Quaternary kinematics of the Leech River fault: implications for forearc strain accumulation in northern Cascadia. *Bulletin of the Seismological Society of America*, 111(2): 1110–1138, 2021. doi: 10.1785/0120200204.

Harrichhausen, N., Morell, K. D., Regalla, C., Lynch, E. M., and Leonard, L. J. Eocene terrane accretion in northern Cascadia recorded by brittle left-lateral slip on the San Juan fault. *Tectonics*, 41(10):e2022TC007317, 2022. doi: 10.1029/2022TC007317.

Harrichhausen, N., Audin, L., Baize, S., Johnson, K. L., Beauval, C., Jarrin, P., Marconato, L., Rolandone, F., Jomard, H., Nocquet, J., Alvarado, A., and Mothes, P. A. Fault source models show slip rates measured across the width of the entire fault zone best represent the observed seismicity of the Pallatanga–Puna Fault, Ecuador. *Seismological Research Letters*, 95(1):95–112, 2023a.

doi: 10.1785/0220230217.

Harrichhausen, N., Finley, T., Morell, K. D., Regalla, C., Bennett, S. E. K., Leonard, L. J., Nissen, E., McLeod, E., Lynch, E. M., Salomon, G., and Sethanant, I. Discovery of an active forearc fault in an urban region: Holocene rupture on the XEOLXELEK-Elk Lake Fault, Victoria, British Columbia, Canada. *Tectonics*, 42 (12):e2023TC008170, 2023b. doi: 10.1029/2023TC008170.

Harrichhausen, N., Morell, K. D., and Regalla, C. Inner forearc faults in northern Cascadia do not accommodate elastic strain driven by the megathrust seismic cycle. *Seismica*, 2(4), 2024. doi: 10.26443/seismica.v2i4.1177.

Hatem, A. E., Cooke, M. L., and Toeneboehn, K. Strain localization and evolving kinematic efficiency of initiating strike-slip faults within wet kaolin experiments. *Journal of Structural Geology*, 101:96–108, 2017. doi: 10.1016/j.jsg.2017.06.011.

Hatem, A. E., Reitman, N. G., Briggs, R. W., Gold, R. D., Thompson Jobe, J. A., and Burgette, R. J. Western U.S. geologic deformation model for use in the U.S. National Seismic Hazard Model 2023. *Seismological Research Letters*, 93(6):3053–3067, 2022. doi: 10.1785/0220220154.

Hatem, A. E., Briggs, R. W., and Gold, R. D. How does the onset of offset influence geologic slip rates? *Seismological Research Letters*, 96(1):363–376, 2025. doi: 10.1785/0220240096.

Herman, M. W. and Govers, R. Stress evolution during the megathrust earthquake cycle and its role in triggering extensional deformation in subduction zones. *Earth and Planetary Science Letters*, 544:116379, 2020. doi: 10.1016/j.epsl.2020.116379.

Hodgson, E. British Columbia earthquake June 23rd, 1946. *The Journal of The Royal Astronomical Society of Canada*, 40(8): 285–319, 1946.

Johnston, S. T. and Acton, S. The Eocene Southern Vancouver Island Orocline-a response to seamount accretion and the cause of fold-and-thrust belt and extensional basin formation. *Tectonophysics*, 365(1-4):165–183, 2003. doi: 10.1016/S0040-1951(03)00021-0.

JPL, N. NASA Shuttle Radar Topography Mission Global 1 arc second, 2013. doi: 10.5067/MEaSUREs/SRTM/SRTMGL1.003. Dataset.

Koral, H. Surface rupture and rupture mechanism of the October 1, 1995 (Mw=6.2) Dinar earthquake, SW Turkey. *Tectonophysics*, 327(1):15–24, 2000. doi: 10.1016/S0040-1951(00)00159-1.

Kreemer, C., Blewitt, G., and Klein, E. C. A geodetic plate motion and Global Strain Rate Model. *Geochemistry, Geophysics, Geosystems*, 15(10):3849–3889, 2014. doi: 10.1002/2014GC005407.

Lagerbäck, R. Late Quaternary faulting and paleoseismicity in northern Fennoscandia, with particular reference to the Lansjärv area, northern Sweden. *Geologiska Föreningen i Stockholm Förhandlingar*, 112(4):333–354, 1990. doi: 10.1080/11035899009452733.

Lamontagne, M., Halchuk, S., Cassidy, J. F., and Rogers, G. C. Significant Canadian earthquakes 1600-2017. Technical Report 8285, Natural Resources Canada, 2018. doi: 10.4095/311183.

Lane, E. Report of the subcommittee on sediment terminology. *Transactions of the American Geophysical Union*, 28(6):936–938, 1947.

Li, C., Pang, J., and Zhang, Z. Characteristics, geometry, and segmentation of the surface rupture associated with the 14 April 2010 Yushu Earthquake, Eastern Tibet, China. *Bulletin of the Seismological Society of America*, 102(4):1618–1638, 2012. doi: 10.1785/0120110261.

Li, G., Liu, Y., Regalla, C., and Morell, K. D. Seismicity relocation and fault structure near the Leech River Fault Zone, southern Vancouver Island. *Journal of Geophysical Research : Solid Earth*, 123:2841–2855, 2018a. doi: 10.1002/2017JB015021.

Li, S., Wang, K., Wang, Y., Jiang, Y., and Dosso, S. E. Geodetically inferred locking state of the Cascadia megathrust based on a viscoelastic Earth model. *Journal of Geophysical Research: Solid Earth*, 123(9):8056–8072, 2018b. doi: 10.1029/2018JB015620.

Li, Z., Bruhn, R. L., Pavlis, T. L., Vorkink, M., and Zeng, Z. Origin of sackung uphill-facing scarps in the Saint Elias orogen, Alaska: LIDAR data visualization and stress modeling. *Bulletin of the Geological Society of America*, 122(9-10):1585–1589, 2010. doi: 10.1130/B30019.1.

Loveless, J. P., Allmendinger, R. W., Pritchard, M. E., and González, G. Normal and reverse faulting driven by the subduction zone earthquake cycle in the northern Chilean fore arc. *Tectonics*, 29 (2):1–16, 2010. doi: 10.1029/2009TC002465.

Lynch, E. M., Regalla, C., Morell, K. D., Harrichhausen, N., and Leonard, L. J. Three-dimensional offsets of geomorphic piercing lines displaced by the Quaternary-active Beaufort Range fault, northern Cascadia forearc, BC, Canada, 2025. doi: https://doi.org/10.5061/dryad.nvx0k6dvc. Dataset.

Madsen, J. K., Thorkelson, D. J., Friedman, R. M., and Marshall, D. D. Cenozoic to recent plate configurations in the Pacific Basin: Ridge subduction and slab window magmatism in Western North America. *Geosphere*, 2(1):11–34, 2006. doi: 10.1130/GES00020.1.

Marrett, R. and Allmendinger, R. W. Kinematic analysis of fault-slip data. *Journal of Structural Geology*, 12:973–986, 1990. doi: 10.1016/0191-8141(90)90093-E.

Massey, N., Friday, S., Riddell, J., and Dumais, S. Geology of the Port Alberni-Nanaimo Lakes area, 1991.

Mathews, W. H. Landslides of central Vancouver Island and the 1946 earthquake. *Bulletin of the Seismological Society of America*, 69(2):445–450, 1979. doi: 10.1785/BSSA0690020445.

Mazzotti, S., Dragert, H., Hyndman, R. D., Miller, M., and Henton, J. A. GPS deformation in a region of high crustal seismicity: N. Cascadia forearc. *Earth and Planetary Science Letters*, 198(1-2): 41–48, 2002. doi: 10.1016/S0012-821X(02)00520-4.

McCaffrey, R., King, R. W., Payne, S. J., and Lancaster, M. Active tectonics of northwestern U.S. inferred from GPS-derived surface velocities. *Journal of Geophysical Research: Solid Earth*, 118(2): 709–723, 2013. doi: 10.1029/2012JB009473.

McCalpin, J. P. Criteria for determining the seismic significance of sackungen and other scarplike landforms in mountainous regions. Technical Report NUREG/CR-5503, U.S. Nuclear Regulatory Commission, 1990.

McCalpin, J. P. Tectonic geomorphology and Holocene paleoseismicity of the Molesworth section of the Awatere Fault, South Island, New Zealand. *New Zealand Journal of Geology and Geophysics*, 39(1):33–50, 1996. doi: 10.1080/00288306.1996.9514693.

Morell, K. D., Regalla, C., Leonard, L. J., Amos, C. B., and Levson, V. Quaternary rupture of a crustal fault beneath Victoria, British Columbia, Canada. *GSA Today*, 27(3-4):4–10, 2017. doi: 10.1130/GSATG291A.1.

Morell, K. D., Regalla, C., Amos, C. B., Bennett, S. E., Leonard, L. J., Graham, A., Reedy, T., Levson, V., and Telka, A. Holocene surface rupture history of an active forearc fault redefines seismic hazard in southwestern British Columbia, Canada. *Geophysical Research Letters*, 45(21):11,605–11,611, 2018. doi: 10.1029/2018GL078711.

Morell, K. D., Styron, R., Stirling, M., Griffin, J., Archuleta, R., and Onur, T. Seismic hazard analyses from geologic and geomorphic data: current and future challenges. *Tectonics*, 39(10):

e2018TC005365, 2020. doi: 10.1029/2018TC005365.

Mosher, D. C. and Hewitt, A. T. Late Quaternary deglaciation and sea-level history of eastern Juan de Fuca Strait, Cascadia. *Quaternary International*, 121(1):23–39, 2004. doi: 10.1016/j.quaint.2004.01.021.

Muir-Wood, R. Deglaciation Seismotectonics: a principal influence on intraplate seismogenesis at high latitudes. *Quaternary Science Reviews*, 19(14):1399–1411, 2000. doi: 10.1016/S0277-3791(00)00069-X.

Mulder, T. Small earthquakes in southwestern British Columbia (1975-1991). Master's thesis, University of Victoria, 1995.

Muller, J. E. and Carson, D. J. T. Geology and mineral deposits of Alberni map area, British Columbia (92F). *Geological Survey of Canada Paper*, 1969.

Natural Resources Canada. Canadian Digital Elevation Model 1945-2011, 2013.

Nelson, A. R., Johnson, S. Y., Kelsey, H. M., Wells, R. E., Sherrod, B. L., Pezzopane, S. K., Bradley, L.-A., Koehler, R. D., and Bucknam, R. C. Late Holocene earthquakes on the Toe Jam Hill fault, Seattle fault zone, Bainbridge Island, Washington. *Geological Society of America Bulletin*, 115(11):1388, 2003. doi: 10.1130/B25262.1.

Nelson, A. R., Personius, S. F., Wells, R. E., Schermer, E. R., Bradley, L. A., Buck, J., and Reitman, N. Holocene earthquakes of magnitude 7 during westward escape of the Olympic Mountains, Washington. *Bulletin of the Seismological Society of America*, 107 (5):2394–2415, 2017. doi: 10.1785/0120160323.

Personius, S. F., Briggs, R. W., Nelson, A. R., Schermer, E. R., Zebulon Maharrey, J., Sherrod, B. L., Spaulding, S. A., and Bradley, L. A. Holocene earthquakes and right-lateral slip on the left-lateral Darrington-Devils Mountain fault zone, northern Puget Sound, Washington. *Geosphere*, 10(6):1482–1500, 2014. doi: 10.1130/GES01067.1.

Philip, H. and Meghraoui, M. Structural analysis and interpretation of the surface deformations of the El Asnam Earthquake of October 10, 1980. *Tectonics*, 2(1):17–49, 1983. doi: 10.1029/TC002i001p00017.

Regalla, C., Fisher, D. M., Kirby, E., Oakley, D., and Taylor, S. Slip inversion along inner fore-arc faults, Eastern Tohoku, Japan. *Tectonics*, 36(11):2647–2668, 2017. doi: 10.1002/2017TC004766.

Reimer, P. J., Austin, W. E., Bard, E., Bayliss, A., Blackwell, P. G., Bronk Ramsey, C., Butzin, M., Cheng, H., Edwards, R. L., Friedrich, M., Grootes, P. M., Guilderson, T. P., Hajdas, I., Heaton, T. J., Hogg, A. G., Hughen, K. A., Kromer, B., Manning, S. W., Muscheler, R., Palmer, J. G., Pearson, C., Van Der Plicht, J., Reimer, R. W., Richards, D. A., Scott, E. M., Southon, J. R., Turney, C. S., Wacker, L., Adolphi, F., Büntgen, U., Capano, M., Fahrni, S. M., Fogtmann-Schulz, A., Friedrich, R., Köhler, P., Kudsk, S., Miyake, F., Olsen, J., Reinig, F., Sakamoto, M., Sookdeo, A., and Talamo, S. The IntCal20 Northern Hemisphere radiocarbon age calibration curve (0-55 cal kBP). *Radiocarbon*, 62(4):725–757, 2020. doi: 10.1017/RDC.2020.41.

Reitman, N. G., Mueller, K. J., Tucker, G. E., Gold, R. D., Briggs, R. W., and Barnhart, K. R. Offset channels may not accurately record strike-slip fault displacement: Evidence from landscape evolution models. *Journal of Geophysical Research: Solid Earth*, 124 (12):13427–13451, 2019. doi: 10.1029/2019JB018596.

Reitman, N. G., Klinger, Y., Briggs, R. W., and Gold, R. D. Climatic influence on the expression of strike-slip faulting. *Geology*, 51: 18–22, 2023. doi: 10.1130/G50393.1.

Riller, U., Clark, M. D., Daxberger, H., Doman, D., Lenauer, I., Plath, S., and Santimano, T. Fault-slip inversions: Their importance in terms of strain, heterogeneity, and kinematics of brittle deformation. *Journal of Structural Geology*, 101:80–95, 2017. doi: 10.1016/j.jsg.2017.06.013.

Rodriguez Padilla, A. M., Oskin, M. E., Brodsky, E. E., Dascher-Cousineau, K., Herrera, V., and White, S. The influence of fault geometrical complexity on surface rupture length. *Geophysical Research Letters*, 51(20):e2024GL109957, 2024. doi: 10.1029/2024GL109957.

Rogers, G. C. Earthquake fault plane solutions near Vancouver Island. *Canadian Journal of Earth Sciences*, 16(3):523–531, 1979. doi: 10.1139/e79-047.

Rogers, G. C. and Hasegawa, H. S. A second look at the British Columbia earthquake of June 23, 1946. *Bulletin of the Seismological Society of America*, 68(3):653–676, 1978. doi: 10.1785/BSSA0680030653.

Ryder, J. M. The stratigraphy and morphology of para-glacial alluvial fans in South-central British Columbia. *Canadian Journal of Earth Sciences*, 8(2):279–298, 1971. doi: 10.1139/e71-027.

Scharer, K., Salisbury, J., Arrowsmith, R., and Rockwell, T. Southern San Andreas fault evaluation field activity: approaches to measuring small geomorphic offsets–challenges and recommendations for active fault studies. *Seismological Research Letters*, 85:68–76, 2014. doi: 10.1785/0220130108.

Schermer, E. R., Amos, C. B., Duckworth, W. C., Nelson, A. R., Angster, S., Delano, J., and Sherrod, B. L. Postglacial Mw 7.0–7.5 earthquakes on the North Olympic fault zone, Washington. *Bulletin of the Seismological Society of America*, 111(1):490–513, 2021. doi: 10.1785/0120200176.

Sherrod, B. L., Blakely, R. J., Weaver, C. S., Kelsey, H. M., Barnett, E., Liberty, L., Meagher, K. L., and Pape, K. Finding concealed active faults: Extending the southern Whidbey Island fault across the Puget Lowland, Washington. *Journal of Geophysical Research: Solid Earth*, 113(5):1–25, 2008. doi: 10.1029/2007JB005060.

Sherrod, B. L., Barnett, E., Schermer, E. R., Kelsey, H. M., Hughes, J. F., Foit, F. F., Weaver, C. S., Haugerud, R. A., and Hyatt, T. Holocene tectonics and fault reactivation in the foothills of the north Cascade Mountains, Washington. *Geosphere*, 9(4): 827–852, 2013. doi: 10.1130/GES00880.1.

Sieh, K. E. Prehistoric large earthquakes produced by slip on the San Andreas Fault at Pallett Creek, California. *Journal of Geophysical Research*, 83(B8):3907, 1978. doi: 10.1029/JB083iB08p03907.

Slawson, W. F. and Savage, J. C. Geodetic deformation associated with the 1946 Vancouver Island, Canada, earthquake. *Bulletin of the Seismological Society of America*, 69(5):1487–1496, 1979. doi: 10.1785/BSSA0690051487.

Steffen, R., Steffen, H., Wu, P., and Eaton, D. W. Stress and fault parameters affecting fault slip magnitude and activation time during a glacial cycle. *Tectonics*, 33(7):1461–1476, 2014. doi: 10.1002/2013TC003450.

Stuiver, M. and Polach, H. A. Reporting of ^{14}C data. *Radiocarbon*, 19(3):355–363, 1977.

Styron, R. The impact of earthquake cycle variability on neotectonic and paleoseismic slip rate estimates. *Solid Earth*, 10(1): 15–25, 2019. doi: 10.5194/se-10-15-2019.

Thenhaus, P. and Campbell, K. Seismic hazard analysis. In Chen, W.-F. and Scawthorn, C., editors, *Earthquake Engineering Handbook*, New directions in civil engineering. CRC Press, Boca Raton, FL, 2002.

Toda, S., Stein, R. S., and Lin, J. Widespread seismicity excitation throughout central Japan following the 2011 M=9.0 Tohoku earthquake and its interpretation by Coulomb stress transfer. *Geophysical Research Letters*, 38(7), 2011. doi: 10.1029/2011GL047834.

U.S. Geological Survey. Quaternary fault and fold database for the

United States, 2018. https://www.usgs.gov/natural-hazards/earthquake-hazards/faults.

van Wijk, J., Axen, G., and Abera, R. Initiation, evolution and extinction of pull-apart basins: Implications for opening of the Gulf of California. *Tectonophysics*, 719-720:37–50, 2017. doi: 10.1016/j.tecto.2017.04.019.

Walton, M. A., Staisch, L. M., Dura, T., Pearl, J. K., Sherrod, B., Gomberg, J., Engelhart, S., Tréhu, A., Watt, J., Perkins, J., Witter, R. C., Bartlow, N., Goldfinger, C., Kelsey, H., Morey, A. E., Sahakian, V. J., Tobin, H., Wang, K., Wells, R., and Wirth, E. Toward an integrative geological and geophysical view of Cascadia subduction zone earthquakes. *Annual Review of Earth and Planetary Sciences*, 49(1):367–398, 2021. doi: 10.1146/annurev-earth-071620-065605.

Wang, K. Stress-strain 'paradox', plate coupling, and forearc seismicity at the Cascadia and Nankai subduction zones. *Tectonophysics*, 319(4):321–338, 2000. doi: 10.1016/S0040-1951(99)00301-7.

Wang, K., Mulder, T., Rogers, G. C., and Hyndman, R. Case for very low coupling stress on the Cascadia Subduction Fault. *Journal of Geophysical Research*, 100, 1995. doi: 10.1029/95JB00516.

Wells, D. L. and Coppersmith, K. J. New empirical relationships among magnitude, rupture length, rupture width, rupture area, and surface displacement. *Bulletin of the Seismological Society of America*, 84(4):974–1002, 1994. doi: 10.1785/BSSA0840040974.

Wells, R. E., Weaver, C. S., and Blakely, R. J. Fore-arc migration in Cascadia and its neotectonic significance. *Geology*, 26(8):759–762, 1998. doi: 10.1130/0091-7613(1998)026<0759:FAMICA>2.3.CO;2.

Wesnousky, S. G. Seismological and structural evolution of strike-slip faults. *Nature*, 335(6188):340–343, 1988. doi: 10.1038/335340a0.

Wesnousky, S. G. Displacement and geometrical characteristics of earthquake surface ruptures: Issues and implications for seismic-hazard analysis and the process of earthquake rupture. *Bulletin of the Seismological Society of America*, 98(4):1609–1632, 2008. doi: 10.1785/0120070111.

Working Group on California Earthquake Probabilities. *Probabilities of Large Earthquakes in the San Francisco Bay Region, California*. Department of the Interior, U.S. Geological Survey, 1990.

Yorath, C. J., Clowes, R. M., Green, A. G., Sutherland-Brown, A., Brandon, M. T., Massey, N. W., Spencer, C., Kanasewich, E. R., and Hyndman, R. D. Lithoprobe - Phase 1: southern Vancouver Island: preliminary analyses of reflection seismic profiles and surface geological studies. In *Current Research, Part A*, number 85-1A in Geological Survey of Canada Paper, pages 543–554. Geological Survey of Canada, 1985a.

Yorath, C. J., Green, A. G., Clowes, R. M., Brown, A. S., Brandon, M. T., Kanasewich, E. R., and Spencer, C. Lithoprobe, southern Vancouver Island: Seismic reflection sees through Wrangellia to the Juan de Fuca plate. *Geology*, 13(13):759–762, 1985b. doi: 10.1130/0091-7613(1985)13<759.

Yuan, Z., Li, T., Su, P., Sun, H., Ha, G., Guo, P., Chen, G., and Thompson Jobe, J. Large surface-rupture gaps and low surface fault slip of the 2021 Mw 7.4 Maduo earthquake along a low-activity strike-slip Fault, Tibetan Plateau. *Geophysical Research Letters*, 49(6):e2021GL096874, 2022. doi: 10.1029/2021GL096874.

Zielke, O. and Arrowsmith, J. R. LaDiCaoz and LiDARimager—MATLAB GUIs for LiDAR data handling and lateral displacement measurement. *Geosphere*, 8(1):206–221, 2012. doi: 10.1130/GES00686.1.

Zielke, O., Arrowsmith, J. R., Ludwig, L. G., and Akçiz, S. O. Slip in the 1857 and earlier large earthquakes along the Carrizo Plain, San Andreas Fault. *Science*, 327(5969):1119–1122, 2010. doi: 10.1126/science.1182781.